

SURROGATE-ASSISTED GLOBAL SENSITIVITY ANALYSIS OF A HYBRID-DIMENSIONAL STOKES–BRINKMAN–DARCY MODEL ^{*, **, ***}

LINHENG RUAN¹, ILJA KRÖKER², SERGEY OLADYSHKIN² AND IRYNA RYBAK¹

Abstract. Development of new multiscale mathematical models often entails considerable complexity and multiple undetermined parameters, typically arising from closure relations. To enable reliable simulations, one must quantify how uncertain physical parameters influence model predictions. We propose surrogate-assisted global sensitivity analysis that combines computational efficiency with a rigorous assessment of parameter influence. In this work, we analyze the recently proposed hybrid-dimensional Stokes–Brinkman–Darcy model, which describes fluid flows in coupled free-flow and porous-medium systems with arbitrary flow directions at the fluid–porous interface. The model results from vertical averaging and contains several unknown parameters. We perform surrogate-assisted global sensitivity analysis using Sobol’ indices to investigate the sensitivity of the model to variations of physical parameters for two test cases: filtration and splitting flows. However, constructing surrogates for higher-dimensional random fields requires either many training runs or sophisticated sampling strategies. To address this, we compare polynomial chaos surrogates, including sparse and multi-resolution representations, for their efficiency in global sensitivity analysis, using a predefined Sobol’ sequence of training samples. Across the tested cases, multi-resolution approach delivers the most accurate estimation of Sobol’ indices.

2020 Mathematics Subject Classification. 35Q35, 65C20, 76D07, 76M12, 76S05.

February 26, 2026.

1. INTRODUCTION

Fluid flow and transport processes in coupled systems consisting of a free-flow region in contact with a porous medium arise frequently in science and engineering. Examples include surface water infiltration into soil, contaminant transport, industrial drying, blood flow in biological tissues, etc. Since resolving the detailed

Keywords and phrases: Global sensitivity analysis, Sobol’ index, hybrid-dimensional model, data-driven modeling, coupled flow system, porous medium, polynomial chaos expansion, arbitrary multi-resolution polynomial chaos, Sobol’ sequence

* *The first and fourth authors thank the Deutsche Forschungsgemeinschaft (DFG, German Research Foundation) – Project Number 490872182 for the financial support.*

** *The second and third authors thank the Deutsche Forschungsgemeinschaft (DFG, German Research Foundation) – Project Number 535321881 for the financial support.*

*** *The third and fourth authors thank the Deutsche Forschungsgemeinschaft (DFG, German Research Foundation) – Project Number 327154368 – SFB 1313 for the financial support.*

¹ Institute of Applied Analysis and Numerical Simulation, University of Stuttgart, Stuttgart, Germany;
e-mail: linheng.ryan@ians.uni-stuttgart.de & iryna.rybak@ians.uni-stuttgart.de

² Institute for Modelling Hydraulic and Environmental Systems, University of Stuttgart, Stuttgart, Germany;
e-mail: ilja.kroeker@iws.uni-stuttgart.de & sergey.oladyshkin@iws.uni-stuttgart.de

pore-scale geometry is computationally demanding, the free-flow region and the porous-medium domain are typically modeled as two distinct continua separated by a fluid–porous interface. This approach requires either suitable coupling conditions or a dimensionally reduced model at the interface, or alternatively a full-dimensional representation of the transition zone between the two flow domains (Fig. 1). Depending on the application and flow regime, different models can be applied in the two subdomains. In this paper, we focus on the problem most extensively studied over the past 25 years, namely the Stokes equations in the free-flow region coupled with Darcy’s law in the porous medium.

Various coupling strategies for the Stokes–Darcy flow problems have been proposed in the literature [1, 10, 21, 24, 32, 34]. The classical set of interface conditions, which comprise mass conservation across the sharp interface, the balance of normal forces, and a variant of the Beavers–Joseph condition for the tangential velocity component, has been widely used, e.g. [4, 11, 23, 51]. However, these conditions have been shown to lose accuracy for arbitrary flow directions at the fluid–porous interface [13, 57]. To enhance the classical Stokes–Darcy coupling, several generalized formulations have been proposed in recent studies [1, 2, 14, 32, 34, 49, 50, 58, 68]. However, many of these theoretically derived coupling conditions have not been validated for arbitrary flow directions near the fluid–porous interface (e.g., [1, 2, 21, 33]), and some have not been validated at all, largely because certain model parameters remain uncertain and require quantification.

Sensitivity analysis is a widely used tool to estimate the impact of single model parameters or combinations of parameters on the model output. The two commonly used types of sensitivity analysis are *local*, which evaluates the variation of the model output in terms of the variation of the model parameters located in the immediate area of interests, and *global* sensitivity analysis (GSA), such as the Sobol’ [22, 55, 56] or the Shapley [42, 53] indices, which address the variation of the model response over the entire domain of input parameters. For a comprehensive review, we refer the reader to [9, 60]. The present work is based on global (variance-based) sensitivity, specifically Sobol’ indices [55] to account for interactions across the entire parameter domain. However, the classical Monte Carlo (MC) based approach usually leads to very high computational costs in particular for complex numerical models. Therefore, the use of surrogate models can allow us to reduce the computational effort of GSA [9]. Moreover, surrogates based on the orthonormal polynomial representations are attractive because Sobol’ indices can be obtained directly from the spectral coefficients. Specifically, as shown by Sudret [59] and extended to multi-element/multi-resolution settings in [28], polynomial chaos expansion (PCE) and arbitrary multi-resolution polynomial chaos (aMR-PC) compute Sobol’ indices directly from the coefficients of orthonormal (piecewise) polynomials, thereby eliminating additional surrogate evaluations. The idea of using the orthogonal structure of the PCE to compute the Sobol’ sensitivity indices out of polynomial coefficients was initially introduced by Sudret in [59] and later extended to various versions of the sparse PCE by several authors, e.g. [5, 8]. The specifics of using the piecewise polynomial surrogate models for GSA were addressed in [28], where the computation of the Sobol’ sensitivity indices using the aMR-PC-expansion coefficients was introduced. PCE/aMR-PC-assisted GSA is accurate with appropriately chosen training designs [5, 28, 59]. When training data can be generated on demand this is rarely restrictive. However, with given (non-optimal) datasets, PCE-based surrogates can exhibit oscillations (Runge phenomenon), leading to reduced accuracy. This problem can be addressed using several regularization concepts, e.g. [6, 8], at the price of significantly increased computational costs, which become prohibitively high for larger random fields. In this study, we employ the training points generated by a Sobol’ sequence [54] and convert them to the assumed probability distributions based on the quasi-Monte-Carlo (QMC) approach [60]. This design provides a generic, well space-filling training sequence and enables a fair assessment of non-regularized PCE-based surrogates for GSA.

The objective of the present study is to investigate GSA for the hybrid-dimensional Stokes–Brinkman–Darcy model recently derived in [49, 50]. This model is able to accurately describe fluid flows in coupled systems with arbitrary directions to the fluid–porous interface, thereby extending the applicability of the coupled Stokes–Darcy model to a broader range of applications. The model involves five uncertain parameters and has been validated against several test cases in which the pore geometry is known and certain coefficients can be computed from pore-scale information. The validation is carried out through comparisons between pore-scale

and macroscale simulation results. Here, we investigate the Stokes–Brinkman–Darcy model using surrogate-assisted global sensitivity analysis based on Sobol’ indices with respect to five uncertain physical parameters. To demonstrate applicability of the proposed framework, we consider two representative test cases: a filtration problem and a splitting flow problem.

The manuscript is organized as follows. In Section 2, we introduce the flow system of interest, present the coupled mathematical model, specify the parameter ranges together with their probability distributions, and define two different test cases. In Section 3, we outline the variance-based global sensitivity analysis, introduce the fundamentals of PCE/aMR-PC-based surrogate models, and present the PCE/aMR-PC-surrogate-assisted GSA. In Section 4, we address the approximation and analysis of the physical models using PCE/aMR-PC-based surrogate models, introduced in Section 3. The discussion and conclusions follow in Section 5.

2. HYBRID-DIMENSIONAL STOKES–BRINKMAN–DARCY MODEL

2.1. Flow and geometry setting

We consider single-phase, steady-state flows where the Reynolds number is sufficiently low such that inertial effects can be neglected. The fluid is assumed to be incompressible with constant viscosity and it fully saturates the entire flow domain. In the porous-medium region, the material is taken to be homogeneous and non-deformable.

In the coupled fluid–porous problem, the free-flow Ω_{ff} and porous-medium Ω_{pm} regions are two distinct continua with $\overline{\Omega}_{\text{ff}} \cap \overline{\Omega}_{\text{pm}} = \emptyset$. To bridge these two subdomains, we take into account an equi-dimensional transition zone $\Omega_{\text{tr}} = \{\mathbf{s} + t\mathbf{n} \mid \mathbf{s} \in \Gamma, t \in [-d/2, d/2]\}$ between them (Fig. 1, left), where $d > 0$ is the thickness of the transition region, Γ is the hyperplane and \mathbf{n} is the unit normal vector pointing from hyperplane Γ into the free-flow subdomain Ω_{ff} . There are two different interfaces $\gamma_{\text{ff}} = \overline{\Omega}_{\text{tr}} \cap \overline{\Omega}_{\text{ff}}$ and $\gamma_{\text{pm}} = \overline{\Omega}_{\text{tr}} \cap \overline{\Omega}_{\text{pm}}$ on the top and bottom of the transition zone, respectively.

In the hybrid-dimensional setting, the thickness of the transition zone is assumed to be sufficiently small compared to the size of the fluid domain $\overline{\Omega}_{\text{F}} = \overline{\Omega}_{\text{ff}} \cup \overline{\Omega}_{\text{tr}} \cup \overline{\Omega}_{\text{pm}}$. Therefore, we can treat it as a lower-dimensional inclusion and use the complex interface Γ to approximate the transition region (Fig. 1, right). Note that the small gap is still existing between the free-flow region ($\overline{\Omega}_{\text{ff}} \cap \overline{\Omega}_{\text{pm}} = \emptyset$). The mass and momentum are stored in and transferred along the complex interface Γ , which is modeled by averaging the corresponding conservation equations across the transition zone.

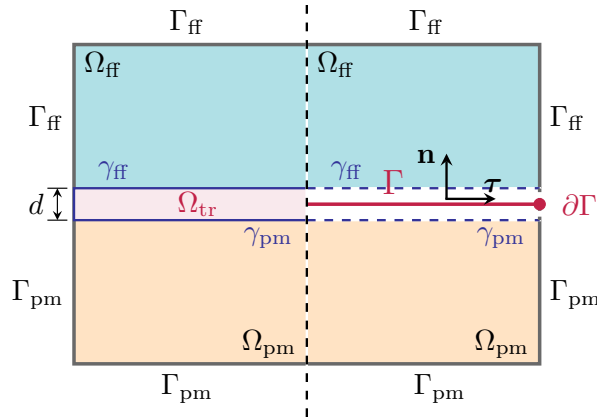


FIGURE 1. Schematic of coupled free-flow and porous-medium systems with a transition region Ω_{tr} (left) and a complex interface Γ (right)

2.2. Model description

In this section, we introduce the recently derived hybrid-dimensional Stokes–Brinkman–Darcy model [48, 50]. The hybrid-dimensional model consists of the Stokes equations in the free-flow region, the averaged Brinkman equations on the complex interface Γ and Darcy’s law in the porous medium. In the free-flow domain, the laminar flow is modeled by the *Stokes equations* involving the mass and momentum conservation

$$\nabla \cdot \mathbf{v}_{\text{ff}} = 0 \quad \text{in } \Omega_{\text{ff}}, \quad (2.1)$$

$$-\nabla \cdot \mathbf{T}(\mathbf{v}_{\text{ff}}, p_{\text{ff}}) = \mathbf{f}_{\text{ff}} \quad \text{in } \Omega_{\text{ff}}. \quad (2.2)$$

Here, \mathbf{v}_{ff} and p_{pm} are the free-flow velocity and pressure, $\mathbf{T}(\mathbf{v}, p) = \mu_{\text{dyn}} \nabla \mathbf{v} - p \mathbf{I}$ is the pseudo stress tensor, μ_{dyn} is the dynamic viscosity, \mathbf{I} is the identity tensor, and \mathbf{f}_{ff} denotes the source term in the free flow. On the external boundary of the free-flow region $\Gamma_{\text{ff}} = \Gamma_{\text{ff}}^{\text{D}} \cup \Gamma_{\text{ff}}^{\text{N}}$, either Dirichlet (D) or Neumann (N) conditions are considered

$$\mathbf{v}_{\text{ff}} = \bar{\mathbf{v}}_{\text{ff}} \quad \text{on } \Gamma_{\text{ff}}^{\text{D}}, \quad \mathbf{T}(\mathbf{v}_{\text{ff}}, p_{\text{ff}}) \cdot \mathbf{n}_{\text{ff}} = \bar{\mathbf{t}}_{\text{ff}} \quad \text{on } \Gamma_{\text{ff}}^{\text{N}}, \quad (2.3)$$

where $\bar{\mathbf{v}}_{\text{ff}}$ and $\bar{\mathbf{t}}_{\text{ff}}$ are the boundary values and \mathbf{n}_{ff} is the outer normal unit vector on the boundary $\Gamma_{\text{ff}}^{\text{N}}$.

In the porous-medium domain, the *Darcy’s law* is used to describe the slow flow

$$\nabla \cdot \mathbf{v}_{\text{pm}} = f_{\text{pm}} \quad \text{in } \Omega_{\text{pm}}, \quad (2.4)$$

$$\mathbf{v}_{\text{pm}} = -\frac{\mathbf{K}_{\text{pm}}}{\mu_{\text{dyn}}} \nabla p_{\text{pm}} \quad \text{in } \Omega_{\text{pm}}, \quad (2.5)$$

where f_{pm} is the source term, \mathbf{v}_{pm} is the porous-medium velocity and p_{pm} is the porous-medium pressure. \mathbf{K}_{pm} is the permeability tensor, which is symmetric positive definite. On the external boundary of the porous medium $\Gamma_{\text{pm}} = \Gamma_{\text{pm}}^{\text{D}} \cup \Gamma_{\text{pm}}^{\text{N}}$, the following conditions are taken into account

$$\mathbf{v}_{\text{pm}} \cdot \mathbf{n}_{\text{pm}} = \bar{v}_{\text{pm}} \quad \text{on } \Gamma_{\text{pm}}^{\text{N}}, \quad p_{\text{pm}} = \bar{p}_{\text{pm}} \quad \text{on } \Gamma_{\text{pm}}^{\text{D}}, \quad (2.6)$$

where \mathbf{n}_{pm} is the outer normal unit vector on the boundary $\Gamma_{\text{pm}}^{\text{N}}$, \bar{v}_{pm} and \bar{p}_{pm} are the boundary data values.

In the full-dimensional setting, the Brinkman equations, which act as a bridge between the Stokes equations and Darcy’s law, are considered in the transition region. In hybrid-dimensional model, the Brinkman equations are averaged in the vertical direction across the transition zone. The *averaged Brinkman equations* on the complex interface yield

$$\mathbf{v}_{\text{ff}} \cdot \mathbf{n}|_{\gamma_{\text{ff}}} - \mathbf{v}_{\text{pm}} \cdot \mathbf{n}|_{\gamma_{\text{pm}}} = -d \frac{\partial V_{\boldsymbol{\tau}}}{\partial \boldsymbol{\tau}} \quad \text{on } \Gamma, \quad (2.7)$$

$$\left(\mathbf{n} \cdot \mathbf{T}(\mathbf{v}_{\text{ff}}, p_{\text{ff}}) \cdot \mathbf{n} - \frac{\mu_{\text{dyn}}}{\sqrt{K_{\Gamma}}} (\boldsymbol{\beta} \mathbf{v}_{\text{ff}}) \cdot \mathbf{n} \right) \Big|_{\gamma_{\text{ff}}} + p_{\text{pm}} \Big|_{\gamma_{\text{pm}}} = d \left(\mu_{\text{dyn}} (\mathbf{K}_{\Gamma}^{-1} \mathbf{V}) \cdot \mathbf{n} - \mu_{\text{eff}} \frac{\partial^2 V_{\mathbf{n}}}{\partial \boldsymbol{\tau}^2} - F_{\mathbf{n}} \right) \quad \text{on } \Gamma, \quad (2.8)$$

$$\begin{aligned} & \left(\mathbf{n} \cdot \mathbf{T}(\mathbf{v}_{\text{ff}}, p_{\text{ff}}) \cdot \boldsymbol{\tau} - \frac{\mu_{\text{dyn}}}{\sqrt{K_{\Gamma}}} (\boldsymbol{\beta} \mathbf{v}_{\text{ff}}) \cdot \boldsymbol{\tau} \right) \Big|_{\gamma_{\text{ff}}} - \frac{\alpha_{\text{BJ}} \mu_{\text{eff}} (6V_{\boldsymbol{\tau}} - 2\mathbf{v}_{\text{ff}} \cdot \boldsymbol{\tau}|_{\gamma_{\text{ff}}})}{\alpha_{\text{BJ}} d + 4\sqrt{K_{\text{pm}}}} \\ & = d \left(\mu_{\text{dyn}} (\mathbf{K}_{\Gamma}^{-1} \mathbf{V}) \cdot \boldsymbol{\tau} - \mu_{\text{eff}} \frac{\partial^2 V_{\boldsymbol{\tau}}}{\partial \boldsymbol{\tau}^2} + \frac{\partial P}{\partial \boldsymbol{\tau}} - F_{\boldsymbol{\tau}} \right) \quad \text{on } \Gamma, \quad (2.9) \end{aligned}$$

where $\mathbf{V} = (V_{\boldsymbol{\tau}}, V_{\mathbf{n}})^{\top}$ and P denote the interfacial velocity and pressure obtained from the vertical averaging of the corresponding quantities across the transition zone, \mathbf{K}_{Γ} is the permeability tensor on the complex interface Γ , $\alpha_{\text{BJ}} > 0$ is the slip coefficient, $\boldsymbol{\beta}$ is the stress jump between Γ and Ω_{ff} and $F_{\mathbf{n}}$, $F_{\boldsymbol{\tau}}$ are the source terms. Note that \mathbf{K}_{Γ} is symmetric positive definite and has the same structure as the porous-medium permeability tensor \mathbf{K} . The corresponding permeability values are $K_{\Gamma} := \|\mathbf{K}_{\Gamma}\|_{\infty}$, $K_{\text{pm}} := \boldsymbol{\tau} \cdot \mathbf{K}_{\text{pm}} \cdot \boldsymbol{\tau}$.

In the hybrid-dimensional Stokes–Brinkman–Darcy problem, additional transmission conditions are required to extrapolate the velocity and the pressure values on γ_{ff} and γ_{pm} and get a closed model. The following *transmission conditions* based on the *a-priori* assumptions on the velocity and pressure profiles across Γ are taken into account

$$\left(\mathbf{n} \cdot \mathbf{T}(\mathbf{v}_{\text{ff}}, p_{\text{ff}}) \cdot \mathbf{n} - \frac{\mu_{\text{dyn}}}{\sqrt{K_{\Gamma}}} (\boldsymbol{\beta} \mathbf{v}_{\text{ff}}) \cdot \mathbf{n} \right) \Big|_{\gamma_{\text{ff}}} = - \frac{\mu_{\text{eff}}}{d} (6V_{\mathbf{n}} - 4\mathbf{v}_{\text{ff}} \cdot \mathbf{n}|_{\gamma_{\text{ff}}} - 2\mathbf{v}_{\text{pm}} \cdot \mathbf{n}|_{\gamma_{\text{pm}}}) - P \quad \text{on } \Gamma, \quad (2.10)$$

$$\left(\mathbf{n} \cdot \mathbf{T}(\mathbf{v}_{\text{ff}}, p_{\text{ff}}) \cdot \boldsymbol{\tau} - \frac{\mu_{\text{dyn}}}{\sqrt{K_{\Gamma}}} (\boldsymbol{\beta} \mathbf{v}_{\text{ff}}) \cdot \boldsymbol{\tau} \right) \Big|_{\gamma_{\text{ff}}} = - \frac{6\mu_{\text{eff}}(\alpha_{\text{BJ}}d + 2\sqrt{K_{\text{pm}}})}{d(\alpha_{\text{BJ}}d + 4\sqrt{K_{\text{pm}}})} V_{\boldsymbol{\tau}} + \frac{4\mu_{\text{eff}}(\alpha_{\text{BJ}}d + 3\sqrt{K_{\text{pm}}})}{d(\alpha_{\text{BJ}}d + 4\sqrt{K_{\text{pm}}})} \mathbf{v}_{\text{ff}} \cdot \boldsymbol{\tau} \Big|_{\gamma_{\text{ff}}} \quad \text{on } \Gamma, \quad (2.11)$$

$$p_{\text{pm}}|_{\gamma_{\text{pm}}} = - \frac{\mu_{\text{eff}}}{d} (6V_{\mathbf{n}} - 2\mathbf{v}_{\text{ff}} \cdot \mathbf{n}|_{\gamma_{\text{ff}}} - 4\mathbf{v}_{\text{pm}} \cdot \mathbf{n}|_{\gamma_{\text{pm}}}) + P \quad \text{on } \Gamma. \quad (2.12)$$

Note that we assume a quadratic velocity and a constant pressure profile across the transition regions in (2.10)–(2.12). The use of a quadratic velocity profile was shown to be a good approximation with the validation against the pore-scale simulation results [49].

On the external boundary nodes of the complex interface $\partial\Gamma = \partial\Gamma^{\text{D}} \cup \partial\Gamma^{\text{N}}$ (Fig. 1, right), the following boundary conditions are taken into account

$$\mathbf{V} = \bar{\mathbf{V}} \quad \text{on } \partial\Gamma^{\text{D}}, \quad \mu_{\text{eff}} \frac{\partial V_{\mathbf{n}}}{\partial \boldsymbol{\tau}} = \bar{T}_{\mathbf{n}}, \quad \mu_{\text{eff}} \frac{\partial V_{\boldsymbol{\tau}}}{\partial \boldsymbol{\tau}} - P = \bar{T}_{\boldsymbol{\tau}} \quad \text{on } \partial\Gamma^{\text{N}}, \quad (2.13)$$

where $\bar{\mathbf{V}}$, $\bar{T}_{\mathbf{n}}$ and $\bar{T}_{\boldsymbol{\tau}}$ are the given boundary data.

Note that in the full-dimensional setting, there are two interfaces, γ_{ff} and γ_{pm} , located at the top and bottom of the transition region (Fig. 1, left), respectively, where different interface conditions are imposed. On the interface γ_{ff} between the free flow and the transition region, we consider the continuity of velocity and the stress jump conditions proposed in [1]. These conditions involve the stress jump tensor $\boldsymbol{\beta}$, the effective viscosity μ_{eff} , and the permeability tensor \mathbf{K}_{Γ} . On the interface γ_{pm} between the transition region and the porous medium, we impose mass conservation, balance of normal forces, and the Beavers–Joseph–Saffman condition [51]. These coupling conditions contains the effective viscosity μ_{eff} , the Beavers–Joseph coefficient α_{BJ} , and the porous-medium permeability tensor \mathbf{K}_{pm} . The coupling conditions (2.7)–(2.12) on the complex interface Γ are derived taking the interface conditions on γ_{ff} and γ_{pm} into account. We refer the reader to [48, 50] for detailed derivation.

2.3. Model parameters

In this work, we make sensitivity analysis for the hybrid-dimensional Stokes–Brinkman–Darcy model (2.1)–(2.13). We restrict ourselves to isotropic porous media: $\mathbf{K}_{\text{pm}} = k_{\text{pm}}\mathbf{I}$, $\mathbf{K}_{\Gamma} = k_{\Gamma}\mathbf{I}$, $\boldsymbol{\beta} = \beta_{\text{sj}}\mathbf{I}$ with $k_{\Gamma} \geq k_{\text{pm}} > 0$, $\beta_{\text{sj}} \geq 0$. Therefore, we obtain $K_{\Gamma} = k_{\Gamma}$ and $K_{\text{pm}} = k_{\text{pm}}$ in Eqs. (2.8)–(2.11). The following parameters in the hybrid-dimensional model are uncertain: stress jump parameter β_{sj} , permeability on the complex interface k_{Γ} , effective viscosity μ_{eff} , slip parameter α_{BJ} , and permeability in the porous medium k_{pm} .

The stress jump parameter β_{sj} is theoretically estimated to be of the order $\mathcal{O}(\sqrt{K_{\Gamma}}/d, d/\sqrt{K_{\Gamma}})$ [39, 40]. This represents a very large range and is not suitable for sensitivity analysis. Through the validation against the pore-scale simulation results [49], the stress jump parameter β_{sj} is treated as fitting parameter and its range can be reduced to $[0, 10]$. We apply a uniform distribution for β_{sj} , since no prior knowledge about its distribution is available.

The values of porous-medium permeability are taken into account $k_{\text{pm}} \in (10^{-8}, 10^{-5})$ to reflect the commonly used porous materials. The log-normal distribution is applied to generate the initial data and reduce it to the interval of interest [28, 46]. The permeability on the complex interface is expected to be larger than or equal to that in the porous-medium region, while retaining the same structural characteristics as in the porous regions.

TABLE 1. Typical values and intervals for the uncertain parameters for the hybrid-dimensional model.

I	Parameter	Interval	Distribution
1	Stress jump β_{sj}	$[0, 10]$	uniform
2	Permeability k_{Γ}	$(10^{-5}, 10^{-2})$	log-normal
3	Effective viscosity μ_{eff}	$[0.1, 10]$	beta
4	Beavers–Joseph α_{BJ}	$(0, 10)$	beta
5	Permeability k_{pm}	$(10^{-8}, 10^{-5})$	log-normal

In this work, we consider the permeability on the complex interface in the range $k_{\Gamma} \in (10^{-5}, 10^{-2})$ and apply the log-normal distribution as for the porous-medium permeability in this interval.

The value of the permeability viscosity μ_{eff} in the Brinkman equations remains a debated issue. Depending on the type of porous medium, numerical simulations have shown that the effective viscosity may be either smaller or larger than the dynamic viscosity μ_{dyn} [62, Chap. 3.4.3]. Based on the volume-averaging approach of the Navier–Stokes equations [39], the effective viscosity is expressed as $\mu_{\text{eff}} = \mu_{\text{dyn}}/\epsilon$, where ϵ denotes the porosity. For applications of the Brinkman model, the porosity is typically in the range $\epsilon \in [0.8, 0.95]$. In highly porous cases, it is often accepted that the effective viscosity should coincide with the dynamic viscosity, i.e., $\mu_{\text{eff}} = \mu_{\text{dyn}}$. In this work, we choose $\mu_{\text{dyn}} = 1$ and select a wider admissible range for the effective viscosity, $\mu_{\text{eff}} \in [0.1, 10]$. To capture plausible physical values, we employ a suitably shaped beta distribution that concentrates most of the probability mass around the interval $[\mu_{\text{dyn}}, \mu_{\text{dyn}}/\epsilon]$, with $\epsilon \in [0.8, 0.95]$.

The slip coefficient α_{BJ} is chosen originally from the Beavers–Joseph condition and the most commonly used value is $\alpha_{\text{BJ}} = 1$ in the literature. We consider a larger range of slip coefficient $\alpha_{\text{BJ}} \in (0, 10)$. We set the mode of the distribution function at $\alpha_{\text{BJ}} = 1$ and use a scaled beta distribution to show the suitable shape of

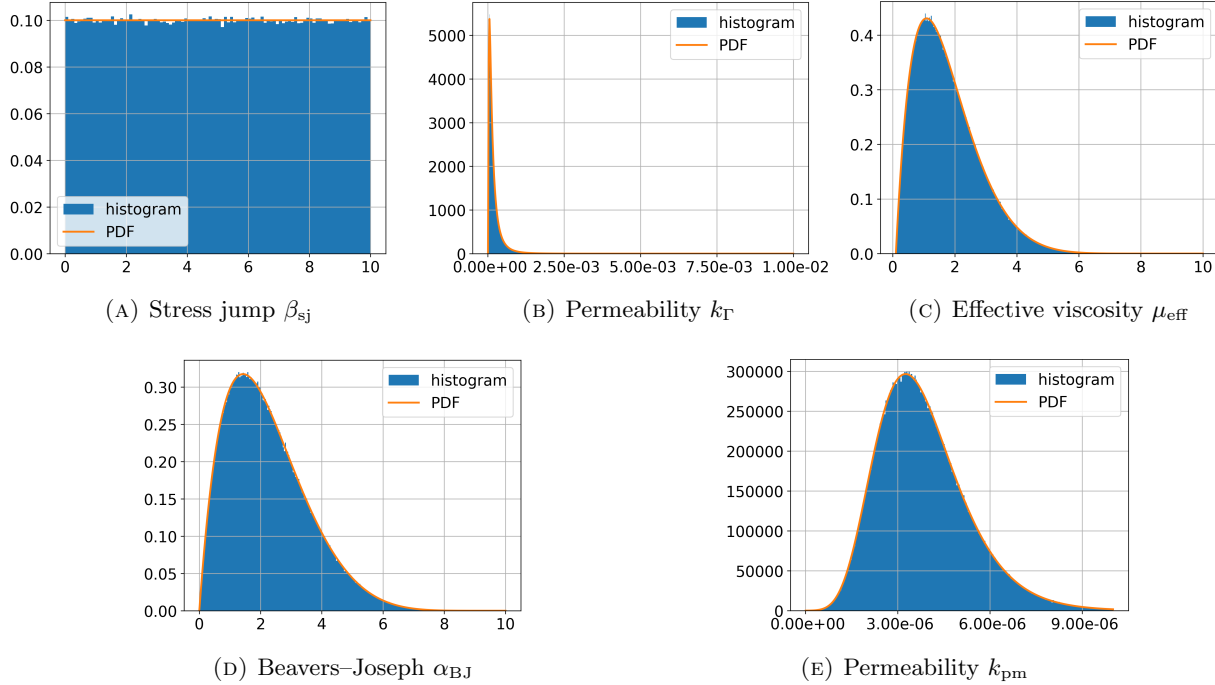


FIGURE 2. Probability density functions (PDF) and histograms of the uncertain parameters.

The source terms are $\mathbf{f}_{\text{ff}} = \mathbf{0}$, $F_{\boldsymbol{\tau}} = F_{\mathbf{n}} = 0$ and $f_{\text{pm}} = 0$. The fluid viscosity is set as $\mu_{\text{dyn}} = 1$. The typical values and the intervals of the stress jump parameter β_{sj} and permeability of the complex interface k_{Γ} in Eqs. (2.8)–(2.11), effective viscosity μ_{eff} in Eqs. (2.8)–(2.12), slip coefficient α_{BJ} in Eqs. (2.9), (2.11) and porous-medium permeability k_{pm} in Eqs. (2.5), (2.9), (2.11) are provided in Tab. 1.

The hybrid-dimensional Stokes–Brinkman–Darcy problems are discretised by the second order finite volume method on staggered rectangular grid of size $h_x \times h_y$ in free-flow and porous-medium regions and second-order finite difference method along the complex interface Γ with the grid size h_x [49]. The grid size is fixed $h = h_x = h_y = 1/100$. The velocity magnitude and the streamlines for the filtration problem are visualized in Fig. 3 (right).

2.5. Test case 2: Splitting flow problem

Generally, the velocity in the free-flow region is much larger than in the porous-medium region. Therefore, as an additional test case, we consider a splitting flow problem, where flow enters the domain from the top boundary and exits through the side boundaries of the free-flow domain. In this setting, the flow in the free-flow region is significantly faster than that in the porous medium. Similar to the case presented in 2.4, different sizes of the outflow boundaries on the external free-flow domain lead to a non-parallel flow to the fluid–porous interface.

In this case, we keep the same geometric setting as the filtration problem in section 2.4, but different settings of boundary conditions are taken into account (Fig. 4, left). On the top of the free-flow region, we prescribe the following “inflow” boundary condition

$$\mathbf{v}_{\text{ff}} = (-0.1 \sin(\pi x_1), 0)^{\top} \quad \text{on } \Gamma_{\text{ff}}^{\text{inflow}} = [0, 1] \times \{1.005\}. \quad (2.19)$$

On the side boundaries of the free-flow domain $\Gamma_{\text{ff}}^{\text{outflow}} = (\{0\} \times [0.505, 1.005]) \cup (\{1\} \times [0.505, 0.755])$, the following “outflow” boundary condition

$$\boldsymbol{\tau} \cdot \mathbf{T}(\mathbf{v}_{\text{ff}}, p_{\text{ff}}) \cdot \boldsymbol{\tau} = 0, \quad \mathbf{v}_{\text{ff}} \cdot \mathbf{n} = 0 \quad \text{on } \Gamma_{\text{ff}}^{\text{outflow}} \quad (2.20)$$

is applied. Similarly, on the boundary nodes of the complex interface Γ , we set

$$\mu_{\text{eff}} \frac{\partial V_{\boldsymbol{\tau}}}{\partial \boldsymbol{\tau}} - P = 0, \quad \mathbf{V}_{\mathbf{n}} = 0 \quad \text{on } \partial\Gamma^{\text{outflow}} = \{(0, 0.5025), (1, 0.5025)\}.$$

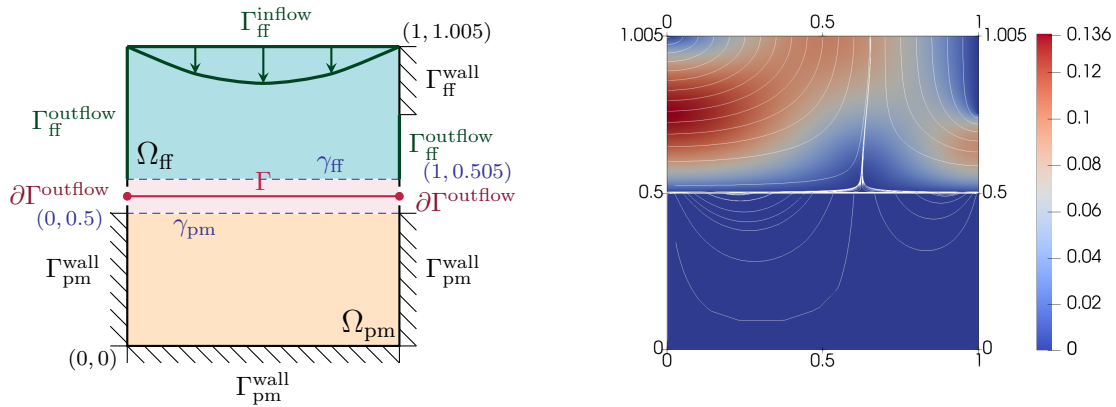


FIGURE 4. Schematic setting (left) and velocity (right) for splitting flow problem.

We take into account “wall” boundary condition (2.18) on the remaining right boundary of the free-flow region $\Gamma_{\text{ff}}^{\text{wall}} = \{1\} \times [0.755, 1.005]$ and the no-slip boundary condition (2.15) on all external boundaries of the porous medium $\Gamma_{\text{pm}}^{\text{wall}} = (\{0\} \times [0, 0.5]) \cup ([0, 1] \times \{0\}) \cup (\{1\} \times [0, 0.5])$.

The source terms are set to $\mathbf{f}_{\text{ff}} = \mathbf{0}$, $F_{\boldsymbol{\tau}} = F_{\mathbf{n}} = 0$, and $f_{\text{pm}} = 0$. The ranges of the stress jump β_{sj} , the interface permeability k_{Γ} , the effective viscosity μ_{eff} , the slip coefficient α , and the porous-medium permeability k_{pm} can be found in Tab. 1. The coupled problem is discretised using the same numerical method as in section 2.4. The velocity for the splitting flow is visualised in Fig. 4 (right).

3. AMR-PC/PCE-ASSISTED GLOBAL SENSITIVITY ANALYSIS.

In this section, we briefly recall variance-based GSA, introduce PCE/aMR-PC surrogate fundamentals, and then show how to compute GSA directly from PCE/aMR-PC coefficients.

3.1. GSA using Sobol’ indices

The origins of variance-based sensitivity analysis go back to the concepts of ANOVA (analysis of variance) originally proposed in the work of Fisher [17, 18] published in the 1920s in the context of agriculture. We briefly recall the ANOVA projection framework to create the link with Sobol’ indices. The core idea is as follows. Let $Y(\boldsymbol{\theta}) := Y(\theta_1, \dots, \theta_M)$ be a square-integrable random variable or a random field. Let P_I , for $I \subseteq \mathcal{N} := \{1, \dots, M\}$ be an orthogonal projection operator satisfying

$$\begin{aligned} P_{\emptyset}Y &:= \mathbb{E}[Y], \\ P_{\{j\}}Y &:= \int Y \, d\mathcal{P}(\boldsymbol{\theta})_{-\{j\}} - P_{\emptyset}Y, \quad j \in \mathcal{N}, \\ P_IY &:= \int Y \, d\mathcal{P}(\boldsymbol{\theta})_{-I} - \sum_{J \subsetneq I} P_JY, \quad I \subseteq \mathcal{N}. \end{aligned}$$

Here, we denote by $\int \cdot \, d\mathcal{P}(\boldsymbol{\theta})_{-\{j\}}$ the integration across all variables θ_i for each $i \in \mathcal{N}$, where $i \neq j$. This leads to the following decomposition of Y :

$$Y(\theta_1, \dots, \theta_M) = P_{\emptyset}Y + \sum_{i=1}^M P_{\{i\}}Y(\theta_i) + \sum_{1 \leq i < j \leq M} P_{\{i,j\}}Y(\theta_i, \theta_j) + \dots = \sum_{I \subseteq \mathcal{N}} P_IY(\boldsymbol{\theta}_I).$$

This also implies the following decomposition of the variance:

$$\sigma^2 = \sum_{I \subseteq \mathcal{N}} \sigma_I^2, \quad \text{where } \sigma_{\emptyset}^2 := 0, \quad \sigma_I^2 := \int (P_IY(\boldsymbol{\theta}))^2 \, d\mathcal{P}(\boldsymbol{\theta}). \quad (3.1)$$

The normalization by the variance leads to the definition of Sobol’ sensitivity indices [55, 56]:

$$S_I := \frac{\sigma_I^2}{\sigma^2}, \quad \text{for } I \subseteq \mathcal{N}.$$

Using Sobol’ sensitivity indices S_I , we can define the total sensitivity indices S_i^T describing the total contribution of each input parameter $i \in \mathcal{N}$ to the variance. The total sensitivity indices are given by

$$S_i^T := \sum_{I \in J_i} S_I, \quad \text{for } J_i = \{(i_1, \dots, i_s) \subseteq \mathcal{N} \mid \exists k, 1 \leq k \leq s, i_k = i\}.$$

3.2. Introduction to PCE and aMR-PC

The concept of PCE, also the use of orthogonal polynomials to build a surrogate model, was initially introduced by Wiener [65] and has since been widely used and extended to date. In the context of uncertainty quantification (UQ), PCE was introduced by Ghanem and Spanos in [20], and since then applied in several areas, e.g. [38, 45, 67]. However, the core idea of the PCE of the second-order random field $Y(\theta) \equiv Y(\mathbf{x}, \theta(\cdot)) \in L^2(\Omega)$ has the following form

$$Y(\mathbf{x}, \theta) \approx \sum_{p=0}^{N_o} c_p(\mathbf{x}) \varphi_p(\theta), \quad c_p(\mathbf{x}) = \langle Y(\mathbf{x}, \cdot), \varphi_p \rangle.$$

Here, N_o is the maximal polynomial degree, and at least in the classical formulation, $c_p(\mathbf{x})$ or c_p denotes the deterministic function or the deterministic coefficient in the case of Y being a random variable, $\langle \cdot, \cdot \rangle$ is equivalent to expectation $\mathbb{E}[\cdot]$ with respect to the probability measure \mathcal{P} , such that orthonormal polynomials φ_p , $p \leq N_o$ satisfy

$$\langle \varphi_p, \varphi_q \rangle = \int_{\Omega} \varphi_p(\theta) \varphi_q(\theta) d\mathcal{P}(\theta) = \delta_{p,q}, \quad p, q = 0, \dots, N_o.$$

The selection or construction of the polynomial basis $\{\varphi_p\}_{p \leq N_o}$ depends directly on the probability distribution of the input parameter θ .

Apart from typical probability distributions like the uniform distribution (associated with Legendre polynomials) or the normal distribution (linked with Hermite polynomials), there exist various construction methods of the corresponding orthogonal polynomials. There is a three-term recurrence relation based on the work of Favard [16]. Another concept is the generalized PCE [67] or the Wiener–Askey polynomial chaos [66], which relies on the Askey polynomials [3]. The third method, which we would like to mention here, is arbitrary polynomial chaos (aPC), which builds orthogonal polynomials directly from the Hankel matrix [41], and therefore relies only on the raw moments of the underlying random variable θ . However, note that the three-term recurrence relation can also be constructed using the Hankel matrix only. Here we refer to [19]. Existence of orthogonal polynomial bases depends on the properties of the raw moments of θ and in particular on the positive definiteness of the Hankel matrix. Here, we refer the readers to [15, 19, 60] for details.

However, independent of the basis construction strategy, one of the drawbacks of the classical PCE approach is their susceptibility to oscillations due to irregularities of the model response (Gibbs’ phenomena) or suboptimal location of the training points (the Runge phenomena). There exist different approaches to reduce or avoid oscillations of the PCE-surrogate model response. First of all, there are the different regularization and sparsity strategies such as LARS-LASSO regression [6, 31, 36], Bayesian sparse PCE [8] or PCE-Kriging [52]. Another approach is the use of multi-resolution [35] and multi-element [64] frameworks, or a combination of the multi-resolution / multi-element framework and regularization [25, 29]. The typical trade-off between both strategies is, at least in our experience, the higher computational effort for training the PCE-surrogate model due to additional optimization steps in case of regularization and higher amount of training samples necessary for building the multi-resolution / multi-element surrogates. Since in our application cases, on the one hand, computational costs of physical models are moderated, and on the other hand, the requirement to deal with a 100×100 random fields yielding 10000 PCE expansions, we omit regularization and proceed with multi-resolution / multi-element PCE Ansatz.

The initial a multi-resolution concept was proposed by Le Maître et al. [35] and later extended to the multi-element by Wan et al. [64]. Since then it has been used in intrusive approaches [7, 26, 44, 61] and later also in non-intrusive approaches [12, 37, 63]. Here, we use arbitrary multi-resolution polynomial chaos (aMR-PC) proposed in [27]. The related Python implementation is available in [30].

Following the idea introduced by Le Maître et al. [35] we split the sample space / dataset Ω into stochastic subdomains (SD) using dyadic decomposition

$$\Omega_{N_r, l} := F_\theta^{-1}([2^{-N_r}l, 2^{-N_r}(l+1)]), \quad l = 0, \dots, 2^{N_r} - 1.$$

Here, $F_\theta(\cdot)$ denotes the cumulative distribution function, and N_r is the number of dyadic refinements. However, by assuming $\Omega \subseteq \mathbb{R}$ (this assumption is valid when working with datasets), we can use the quantile function defined as follows

$$Q_\theta(r) := \inf \{s \in \mathbb{R} \mid r \leq F_\theta(s)\},$$

to obtain SD's

$$\Omega_{N_r, l} = Q_\theta([2^{-N_r}l, 2^{-N_r}(l+1)]), \quad l = 0, \dots, 2^{N_r} - 1.$$

In the next step, we use one of the moment-based methods (aPC [41] or the three-term method described by Gautschi [19]) to construct orthogonal polynomial bases in each SD. By normalizing the polynomials, we obtain the piecewise polynomial basis $\{\varphi_{l,p}^{N_r} \mid l = 0, \dots, 2^{N_r} - 1, p = 0, \dots, N_o\}$, satisfying the orthonormal relation on the whole stochastic domain Ω as follows

$$\langle \varphi_{l,p}^{N_r}, \varphi_{k,q}^{N_r} \rangle = \delta_{l,k} \delta_{p,q}, \quad k, l = 0, \dots, 2^{N_r} - 1, \quad p, q = 0, \dots, N_o.$$

Now we describe the multivariate formulation which provides aMR-PC-surrogate models with multiple uncertain parameters. Let M be the number of uncertain parameters of the physical model. Since in the present work we use the same refinement level $N_r \in \mathbb{N}_0$ for each uncertain parameter, we assume it for notation. Let us define the set of multi-indices $\mathcal{I}_{N_r}^M$ addressing all SD's as follows

$$\mathcal{I}_{N_r}^M := \left\{ \mathbf{l} = (l_1, \dots, l_M)^T \in \mathbb{N}_0^M \mid l_i = 0, \dots, 2^{N_r} - 1, \quad i = 1, \dots, M \right\}.$$

In other words, we obtain $\Omega^M = \bigcup_{\mathbf{l} \in \mathcal{I}_{N_r}^M} \Omega_{N_r, \mathbf{l}}^M$, where $\Omega_{N_r, \mathbf{l}}^M := \Omega_{N_r, l_1} \times \dots \times \Omega_{N_r, l_M}$. To complete the description, we introduce polynomial degree-related multi-indices. Here, we follow the standard notation and use Greek letters $\alpha = (\alpha_1, \dots, \alpha_M)^T \in \mathbb{N}_0^M$. This means that for the multi-dimensional variable $\boldsymbol{\theta} = (\theta_1, \dots, \theta_M)$ the monomial $\boldsymbol{\theta}^\alpha$ has the form $\boldsymbol{\theta}^\alpha = \theta_1^{\alpha_1} \dots \theta_M^{\alpha_M}$. The term $|\alpha| = \alpha_1 + \dots + \alpha_M$ represents the total degree of the monomial $\boldsymbol{\theta}^\alpha$. Using the notation above, we obtain the polynomial basis $\{\Phi_{\mathbf{l}, \alpha}^{N_r} \mid \mathbf{l} \in \mathcal{I}_{N_r}^M, \alpha \in \mathbb{N}_0^M\}$ that is built out of the multivariate piecewise polynomials constructed as follows

$$\Phi_{\mathbf{l}, \alpha}^{N_r}(\boldsymbol{\theta}) := \begin{cases} \prod_{i=1}^M \varphi_{l_i, \alpha_i}^{N_r}(\theta_i), & \boldsymbol{\theta} \in \Omega_{N_r, \mathbf{l}}^M, \\ 0, & \text{else.} \end{cases}$$

Furthermore, multivariate piecewise polynomial functions $\Phi_{\mathbf{l}, \alpha}^{N_r}$ are orthonormal in the sense of

$$\langle \Phi_{\mathbf{l}, \alpha}^{N_r}, \Phi_{\mathbf{m}, \beta}^{N_r} \rangle = \delta_{\mathbf{l}, \mathbf{m}} \delta_{\alpha, \beta}, \quad \text{for } \mathbf{l}, \mathbf{m} \in \mathcal{I}_{N_r}^M, \alpha, \beta \in \mathbb{N}_0^M.$$

Now, we can define the surrogate model $\mathcal{S}^{N_r, N_o} \equiv \mathcal{S}^{N_r, N_o}(\mathbf{x}; \boldsymbol{\theta})$ of the second-order random field $Y \equiv Y(\mathbf{x}; \boldsymbol{\theta})$ using the following aMR-PC expansion

$$\mathcal{S}^{N_r, N_o}(\mathbf{x}; \boldsymbol{\theta}) := \sum_{\mathbf{l} \in \mathcal{I}_{N_r}^M} \sum_{\alpha \in \Lambda^{M, N_o}} Y_{\mathbf{l}, \alpha}^{N_r}(\mathbf{x}) \Phi_{\mathbf{l}, \alpha}^{N_r}(\boldsymbol{\theta}), \quad (3.2)$$

$$Y_{\mathbf{l}, \alpha}^{N_r}(\mathbf{x}) := \langle Y(\mathbf{x}; \cdot), \Phi_{\mathbf{l}, \alpha}^{N_r} \rangle. \quad (3.3)$$

Here, $\Lambda^{M,N_o} = \{\alpha \in \mathbb{N}_0^M \mid |\alpha| \leq N_o\}$ denotes the set of polynomial degrees α truncated by the highest polynomial degree N_o . It should also be mentioned that the aMR-PC expansion defined above is identical to the multivariate PCE in case $N_r = 0$. Despite the fact that the polynomial coefficients $Y_{l,\alpha}^{N_r}$ can be computed according to (3.3) using, for example, a numerical quadrature, the established approach for the non-intrusive method is to use an appropriate least-squares approach, e.g. [27, 59]. In the present work, we apply the Penrose pseudoinverse [43] to solve the linear systems and to obtain the polynomial coefficients. One of the key properties of the PCE / aMR-PC based surrogates, which is also relevant for the present work, is the calculation of the mean $\mu_{\mathcal{S}^{N_r, N_o}}$ and variance $\sigma_{\mathcal{S}^{N_r, N_o}}^2$ of the surrogate $\mathcal{S}^{N_r, N_o}(\cdot)$ using only the polynomial coefficients

$$\mu_{\mathcal{S}^{N_r, N_o}} := \mathbb{E}[\mathcal{S}^{N_r, N_o}] = \sum_{l \in \mathcal{I}_{N_r}^M} Y_l^{N_r} \langle \Phi_{l,0}^{N_r}, \Phi_{0,0}^0 \rangle = \sum_{l \in \mathcal{I}_{N_r}^M} Y_l^0 \cdot 2^{-MN_r/2}, \quad (3.4)$$

$$\sigma_{\mathcal{S}^{N_r, N_o}}^2 := \sigma^2[\mathcal{S}^{N_r, N_o}] = \sum_{l \in \mathcal{I}_{N_r}^M} \sum_{\alpha \in \Lambda^{M, N_o}} \left(Y_{l,\alpha}^{N_r} \right)^2 - \mu_{\mathcal{S}^{N_r, N_o}}^2. \quad (3.5)$$

The size of the linear system that must be solved for the training of the surrogate model $\mathcal{S}^{N_r, N_o}(\cdot)$ is given by the amount of training samples and the number N_{cf} of polynomial coefficients $Y_{l,\alpha}^{N_r}$. There is a clear dependence of the necessary number of training samples on N_{cf} . However, the number of polynomial coefficients of the full-tensor approach is given by

$$N_{cf} = 2^{MN_r} \frac{(N_o + M)!}{N_o! M!}.$$

Here, the symbol (!) denotes the factorial. Since the number of polynomial coefficients N_{cf} , and therefore also the problem size, rapidly increases in almost each non-trivial setting, the reduction of the system size, called sparsity, was addressed by many researchers. One of the few methods that can be performed on the given training data without additional computational effort is *hyperbolic truncation* [6, 36]. The idea here is to reduce the number of *interaction order terms* by employing the q -norm $\|\alpha\|_q = \left(\sum_{i=1}^M |\alpha_i|^q \right)^{1/q}$ for truncation limited by maximal polynomial degree. More precisely, we replace Λ^{M, N_o} in aMR-PC expansion (3.2) by

$$\Lambda^{M, N_o, q} := \left\{ \alpha \in \mathbb{N}_0^M \mid \|\alpha\|_q \leq N_o \right\}, \quad \text{for } q \in (0, 1].$$

We mention here that in the case $q = 1$ the hyperbolic truncation is equivalent to the classical one, such that $\Lambda^{M, N_o, 1} \equiv \Lambda^{M, N_o}$. For $q < 1$, higher-order and high-interaction terms are preferentially pruned.

3.3. GSA using PCE and aMR-PC expansion coefficients

In this section, we summarize how to compute Sobol' sensitivity indices from PCE/aMR-PC expansion coefficients used in the present work. For a more comprehensive description and validation of the methods, we refer, e.g., to [28, 59]. This subsection connects Section 3.1 (ANOVA) with the surrogate definitions above.

3.3.1. Sobol' sensitivity indices using PCE

Let us start with the calculation of the Sobol' indices using the (global) PCE. Since the basis polynomials of the PCE have global support, we can omit the first sum in Eq. (3.2) and obtain

$$\mathcal{S}^{N_o} \equiv \mathcal{S}^{0, N_o} = \sum_{\alpha \in \Lambda^{M, N_o}} Y_\alpha \Phi_\alpha(\boldsymbol{\theta}),$$

or

$$\mathcal{S}^{N_o, q} \equiv \mathcal{S}^{0, N_o, q} = \sum_{\alpha \in \Lambda^{M, N_o, q}} Y_\alpha \Phi_\alpha(\boldsymbol{\theta}),$$

if the hyperbolic truncation was used. Since $\mathcal{S}^{N_o} \equiv \mathcal{S}^{N_o,1}$ and $\Lambda^{M,N_o} \equiv \Lambda^{M,N_o,1}$, we will proceed with the notation related to the hyperbolic truncation. Now we can exploit the structure of the polynomial degrees of the multivariate PCE to obtain the orthogonal projection operator P_I introduced in Section 3.1. Taking advantage of the fact that the degree of polynomial $\alpha_i = 0$, $i = 1, \dots, M$ corresponds to the mean in the related direction, define the set $\Lambda_I^{M,N_o,q}$ of tuples $\alpha = (\alpha_1, \dots, \alpha_M) \in \mathbb{N}_0^M$ with non-zero entries only in the indices $I = (i_1, \dots, i_s) \subseteq \mathcal{N}$:

$$\Lambda_I^{M,N_o,q} := \left\{ \alpha \in \mathbb{N}_0^M \mid \|\alpha\|_q \leq N_o, \begin{array}{l} \alpha_i > 0, \quad \forall i \in \mathcal{N}, \quad i \in I \\ \alpha_i = 0, \quad \forall i \in \mathcal{N}, \quad i \notin I \end{array} \right\}, \quad I \subseteq \mathcal{N}, q \in (0, 1].$$

For example, it is easy to see that for $\alpha \in \Lambda_{\{i\}}^{M,N_o,q}$ the multivariate polynomial $\Phi_\alpha(\boldsymbol{\theta})$ depends only on the uncertain parameter θ_i . This leads to the Sobol' decomposition of the PCE surrogate model $\mathcal{S}^{N_o,q}$:

$$\mathcal{S}^{N_o,q}(\boldsymbol{\theta}) = \sum_{I \subseteq \mathcal{N}} P_I \mathcal{S}^{N_o,q}(\theta_I) = Y_0 + \sum_{I \subseteq \mathcal{N}} \sum_{\alpha \in \Lambda_I^{M,N_o,q}} Y_\alpha \Phi_\alpha(\boldsymbol{\theta}).$$

Using (3.5) we obtain the Sobol' sensitivity indices $S_I[\mathcal{S}^{N_o,q}]$ of the PCE surrogate model $\mathcal{S}^{N_o,q}$, which approximate the Sobol' sensitivity indices S_I of the random field Y :

$$S_I \approx S_I[\mathcal{S}^{N_o,q}] = \sum_{\alpha \in \Lambda_I^{M,N_o,q}} Y_\alpha^2 \underbrace{\mathbb{E}[\Phi_\alpha^2]}_{=1} / \sigma_{\mathcal{S}^{N_o,q}}^2 = \sum_{\alpha \in \Lambda_I^{M,N_o,q}} Y_\alpha^2 / \sigma_{\mathcal{S}^{N_o,q}}^2, \quad \text{for } I \in \mathcal{N}.$$

Therefore, the total sensitivity index S_i^T , $i \in \mathcal{N}$ can be approximated by

$$S_i^T \approx S_i^T[\mathcal{S}^{N_o,q}] = \sum_{J \in \mathcal{N}, i \in J} S_J[\mathcal{S}^{N_o,q}] = \sum_{J \in \mathcal{N}, i \in J} \sum_{\alpha \in \Lambda_J^{M,N_o,q}} Y_\alpha^2 / \sigma_{\mathcal{S}^{N_o,q}}^2.$$

3.3.2. Sobol' sensitivity indices using aMR-PC

Now, we can extend the idea of the calculation of the Sobol' sensitivity indices directly from the expansion coefficients discussed above to the piecewise polynomial setting of aMR-PC. Here, we skip the step-by-step calculation and refer to [28] where the approach was published. Nevertheless, although the underlying principle of this approach is similar to the PCE scenario, the primary distinction lies in the fact that zero-degree polynomials contribute to the variance when $N_r > 0$.

Again, we define the set of polynomial degree tuples $\alpha \in \mathbb{N}_0^M$ corresponding to the index set $I \subseteq \mathcal{N}$ by

$$\mathring{\Lambda}_I^{M,N_o,q} := \left\{ \alpha = (\alpha_1, \dots, \alpha_M) \in \mathbb{N}_0^M \mid \|\alpha\|_q \leq N_o, \alpha_k = 0, \forall k \in \mathcal{N}, k \notin I \right\}, \quad \text{for } I \subseteq \mathcal{N}, q \in (0, 1].$$

Using this notation, we can write the variance index (given in (3.1)) of the aMR-PC surrogate model as follows

$$\begin{aligned} \sigma_{\mathcal{S}^{N_r,N_o,q},I}^2 := & \sum_{\mathbf{l} \in \mathcal{I}_{N_r}^M} \sum_{\mathbf{m} \in \mathcal{I}_{N_r}^M} \sum_{\alpha \in \mathring{\Lambda}_I^{M,N_o,q}} Y_{\mathbf{l},\alpha}^{N_r} Y_{\mathbf{m},\alpha}^{N_r} 2^{-N_r \#(\mathcal{N} \setminus I)} \delta_{\mathbf{l},\mathbf{m},I} \\ & + \sum_{J \subsetneq I} (-1)^{\#(I \setminus J)} \sum_{\mathbf{l} \in \mathcal{I}_{N_r}^M} \sum_{\mathbf{m} \in \mathcal{I}_{N_r}^M} \sum_{\alpha \in \mathring{\Lambda}_J^{M,N_o,q}} 2^{-N_r \#(\mathcal{N} \setminus J)} \delta_{\mathbf{l},\mathbf{m},J}, \end{aligned}$$

where $\#(A)$ denotes the count of elements in A . Further, we use the notation

$$\delta_{\mathbf{l},\mathbf{m},I} := \begin{cases} 1, & \mathbf{l}_i = \mathbf{m}_i, \forall i \in I, \\ 0, & \text{else.} \end{cases}$$

This allows us to approximate the Sobol' sensitivity indices S_I , $I \subseteq \mathcal{N}$ and the total sensitivity indices S_i^T , $i \in \mathcal{N}$ of the random field Y by

$$S_I \approx S_I[\mathcal{S}^{N_r, N_o, q}] := \frac{\sigma_{\mathcal{S}^{N_r, N_o, q}, I}^2}{\sigma_{\mathcal{S}^{N_r, N_o, q}}^2}, \quad S_i^T \approx S_i^T[\mathcal{S}^{N_r, N_o, q}] := \sum_{J \subseteq \mathcal{N}, i \in J} \frac{\sigma_{\mathcal{S}^{N_r, N_o, q}, J}^2}{\sigma_{\mathcal{S}^{N_r, N_o, q}}^2}.$$

4. NUMERICAL EXPERIMENTS

In this section, we address the approximation and analysis of the physical models described in Section 2.4 and Section 2.5 using PCE/aMR-PC-based surrogate models, introduced in Section 3.

It is known that non-regularized (piecewise) polynomial-based surrogate models provide an accurate surrogate model if the training samples are selected appropriately. Otherwise, at least for higher polynomial degrees, the surrogate model response exhibits oscillatory behavior (Runge phenomenon). In the worst case, this can lead to each surrogate requiring its own tailored training set.

In this study, we evaluate the utility of different polynomial-based surrogate models, presented in Section 3, whether piecewise or classical, that are developed using identical space-filling sequences of training samples. More precisely, we employ QMC Sobol' sequences [54] with training sample sizes between 512 and 16,384, corresponding to 2^9 through 2^{14} samples. This design also allows us to assess the utility of the considered polynomial-based surrogate models when training data are given. In both cases, we assume that the uncertain input parameters of the physical model comply with the probability distributions listed in Tab. 1.

To assess the reliability of the expansion coefficients, we evaluated the L^2 -error of the mean and standard deviation over the domain based on the expansion coefficient of the two quantities of interest (u, v) compared to the quantities based on the MC calculated from 50,000 model evaluations. In order to evaluate the overall accuracy of the surrogate models, we calculate the root mean squared error (RMSE), which indicates the error on the scale of the quantities of interest. Additionally, we compute the relative mean square error (MSE), which is scale-independent due to normalization. Based on this evaluation, we proceed to the GSA based on the expansion coefficients. Here, we consider the spatial distribution of the total sensitivity indices, as well as space-averaged values of the Sobol' and total sensitivity indices. To reduce the influence of numerical noise on the GSA, we exclude areas of vanishing variance ($\sigma^2 < 10^{-10}$) while computing the space-averaged indices.

4.1. Case 1: Postprocessing and evaluation

We begin with the postprocessing and evaluation of the filtration problem introduced in Section 2.4. In this configuration, the prescribed inflow at the bottom boundary drives the fluid in the direction of the complex interface, resulting in an extensive exchange between the porous-medium and free-flow regions (Fig. 3). Consequently, the velocity field $\mathbf{v} = (u, v)^T$ has comparable magnitude in both horizontal and vertical directions.

4.1.1. Mean and variance

We use the mean \mathbb{E} , standard deviation σ , and log-variance $\log \sigma^2$ to characterize the random fields. Figure 5 presents the corresponding statistical moments of the MC solution for horizontal and vertical velocity components, computed using 50,000 realizations. Figure 6 shows the mean, standard deviation, and log-variance obtained with the aMR-PC expansion of the polynomial degree $N_o = 2$ and refinement level $N_r = 1$. The logarithm of the variance enhances the visibility of regions with very small fluctuations that would otherwise be hidden in a linear scale. A comparison of the two figures demonstrates that the aMR-PC results reproduce the MC statistics with high fidelity. This agreement is particularly clear in the log-variance of the velocity components u and v , which highlights regions of very small variance (Fig. 5(E,F), Fig. 6(E,F)).

4.1.2. Accuracy of the approximation

To assess the accuracy of the approximation of the response of the physical models for our quantities of interest (u, v), we use RMSE and relative MSE. We evaluate both metrics across several (piecewise) polynomial-based surrogate models. Despite their definitions being very similar, both metrics are relevant. RMSE uses the same

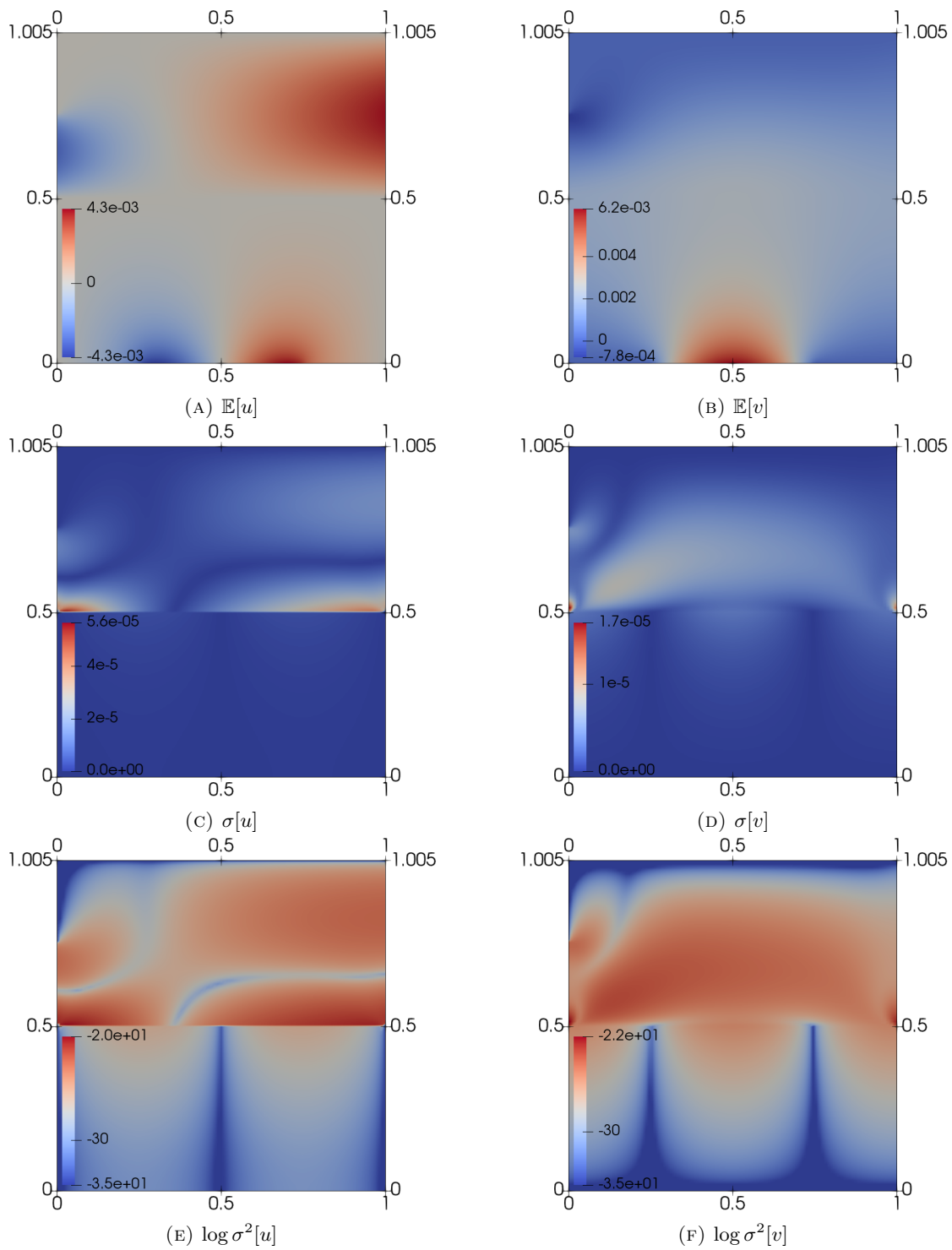


FIGURE 5. Mean, standard deviation and log-variance of the horizontal and vertical velocities (u, v) computed from 50,000 MC samples.

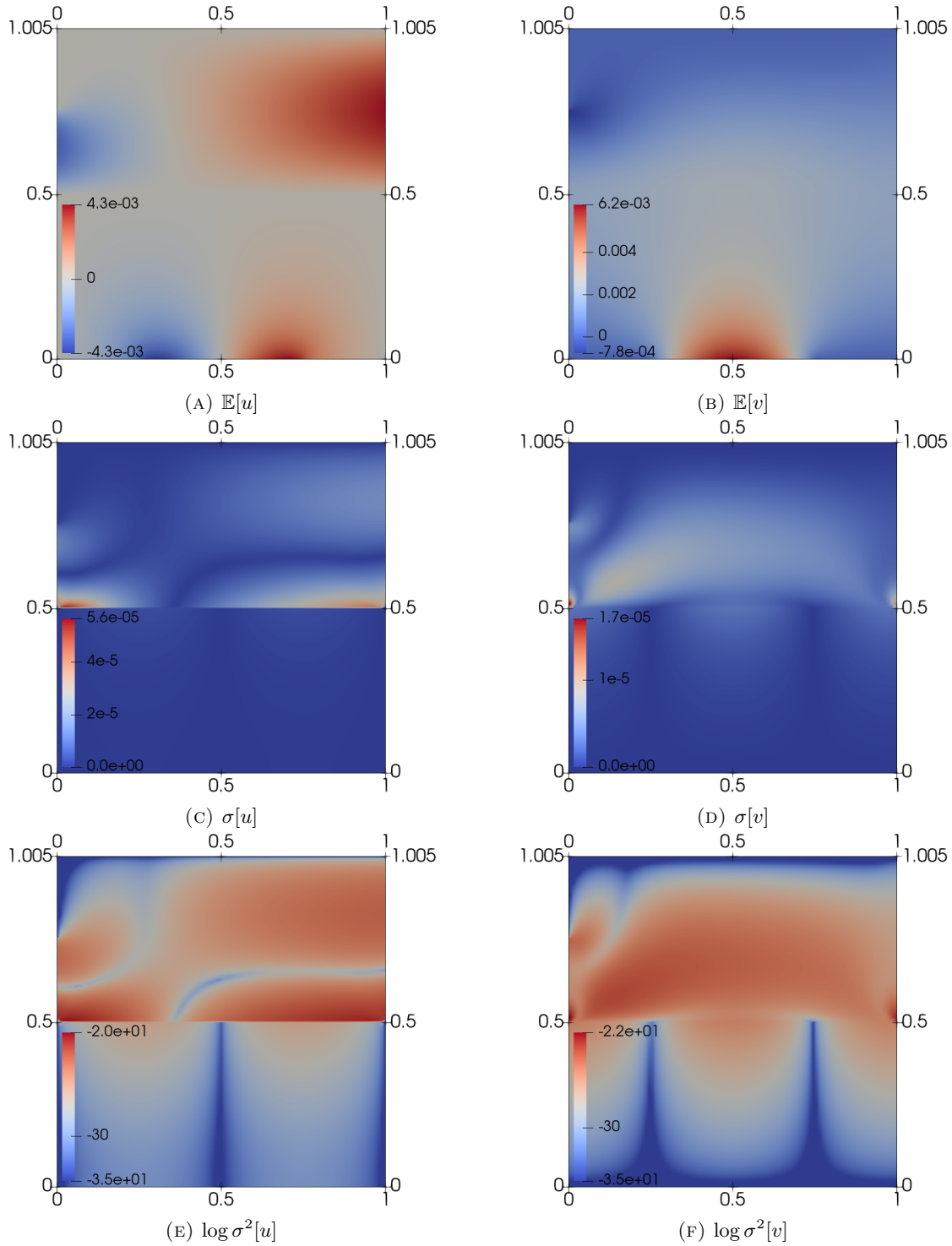


FIGURE 6. Mean, standard deviation and log-variance of the horizontal and vertical velocities (u, v) obtained from aMR-PC-surrogate with $N_r = 1, N_o = 2$, trained on 8192 QMC samples.

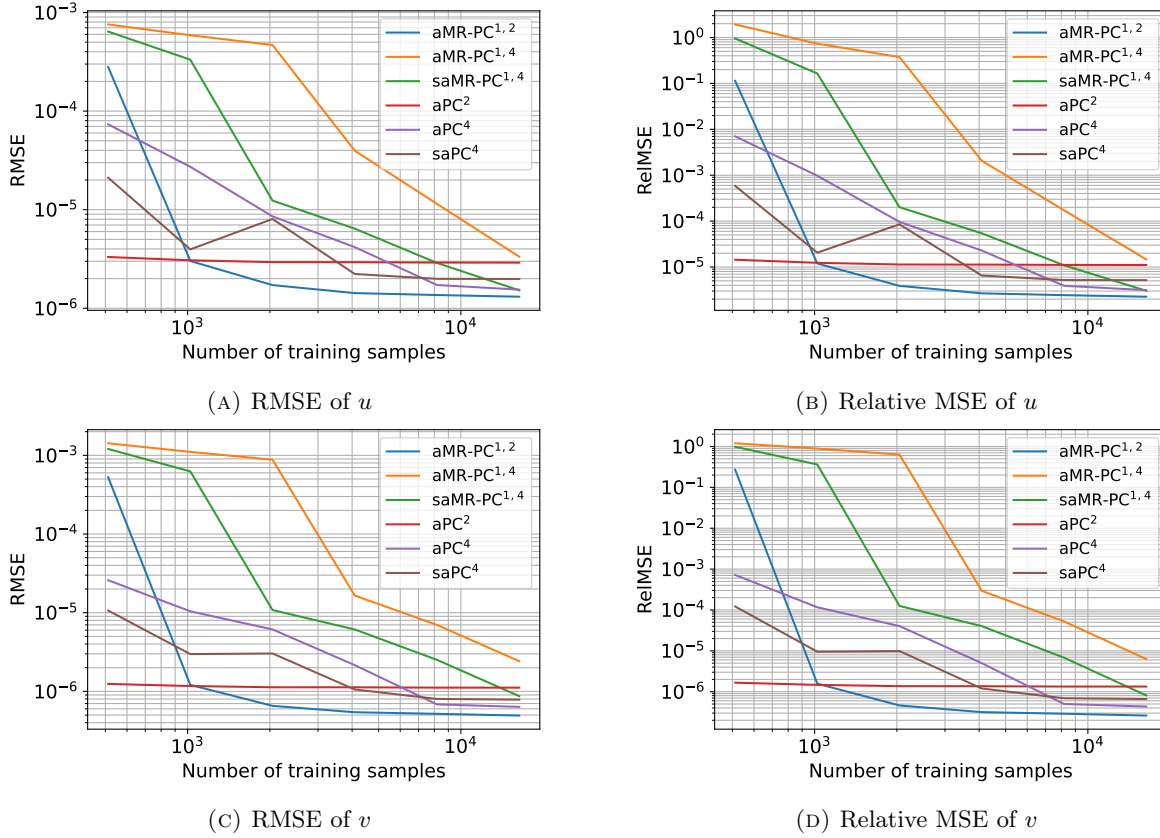


FIGURE 7. Case 1: RMSE and relative MSE error plots for 512, \dots , 16384 training samples.

scale as the underlying quantities and is therefore more relevant from a modeling point of view. However, to compare different quantities of interest, the relative MSE is preferable because of its normalization.

Figure 7 shows the above-mentioned errors evaluated over the whole space domain on 10,000 randomly selected samples. The x -axis is labeled in terms of $2^9, \dots, 2^{14}$ samples used for the training of the surrogate models. Here, we use the following notation: aPC^{N_o} is aPC with the highest polynomial degree N_o , $aMR-PC^{N_r, N_o}$ is aMR-PC with the number of refinements N_r and the highest polynomial degree N_o . Further, $saPC$ and $saMR-PC$ denote the sparse versions of the surrogate models using hyperbolic truncation with $q = 0.75$.

In almost all cases, we observe that the errors decrease with the increasing number of training samples. In Fig. 7, we can see the expected relation between the number of degrees of freedom, the number of required training samples, and the achieved accuracy. More precisely, aPC with $N_o = 2$ obtains its almost highest accuracy with 512 training samples. The $aMR-PC$ with $N_r = 1$ and low polynomial degree $N_o = 2$ provides the most accurate approximation for u and v starting with 2048 training samples. It can also be seen that the convergence is faster if hyperbolic truncation-based sparsity is used.

Since we intend to use the expansion coefficients rather than direct surrogate responses for calculation of the Sobol' coefficients, we also evaluate the accuracy of the approximation of mean and standard deviation of the quantities of interest by using the expansion coefficients given in Eqs. (3.4) and (3.5). The L^2 -error of the approximation of the mean calculated in the whole spatial domain is provided in Tab. 2. Evaluation of the L^2 -error of the approximation of the standard deviation is provided in Tab. 3. In both cases, we use the mean and standard deviation provided by MC computed on 50,000 samples as a reference solution. For both velocity components u and v , aPC with $N_o = 2$ and $aMR-PC$ for $N_r = 1$, $N_o = 2$ (as the number of training samples

TABLE 2. Case 1: L^2 -error of the approximation of the mean (\mathbb{E}).(A) Approximation of the mean of the horizontal velocity component $\mathbb{E}[u]$.

Samples	$N_o = 2$	$N_o = 4$	$N_o = 4/q = 0.75$	$N_r = 1/N_o = 2$	$N_r = 1/N_o = 4$	$N_r = 1/N_o = 4/q = 0.75$
512	1.31e-07	4.08e-06	1.42e-06	1.30e-04	9.16e-04	6.46e-04
1024	5.52e-08	1.44e-06	2.70e-07	9.50e-08	5.07e-04	1.78e-04
2048	1.28e-08	5.73e-07	5.59e-07	4.78e-08	3.58e-04	9.28e-07
4096	7.88e-09	2.57e-07	4.62e-08	2.57e-08	3.94e-06	3.76e-07
8192	1.22e-08	5.96e-08	2.51e-08	9.67e-09	6.38e-07	1.54e-07
16384	1.18e-08	2.42e-08	7.04e-09	5.47e-09	2.40e-07	6.33e-08

(B) Approximation of the mean of the vertical velocity component $\mathbb{E}[v]$.

Samples	$N_o = 2$	$N_o = 4$	$N_o = 4/q = 0.75$	$N_r = 1/N_o = 2$	$N_r = 1/N_o = 4$	$N_r = 1/N_o = 4/q = 0.75$
512	4.32e-08	1.45e-06	6.80e-07	1.76e-04	1.24e-03	8.72e-04
1024	1.87e-08	6.27e-07	1.97e-07	3.25e-08	6.84e-04	2.40e-04
2048	6.70e-09	4.06e-07	2.07e-07	1.70e-08	4.83e-04	4.53e-07
4096	6.67e-09	1.44e-07	5.15e-08	8.92e-09	1.32e-06	1.61e-07
8192	6.63e-09	3.61e-08	2.08e-08	5.27e-09	3.00e-07	8.81e-08
16384	5.96e-09	1.69e-08	9.47e-09	4.52e-09	9.72e-08	3.02e-08

TABLE 3. Case 1: L^2 -error of the approximation of the standard deviation (σ).(A) Approximation of the standard deviation of the horizontal velocity component $\sigma[u]$.

Samples	$N_o = 2$	$N_o = 4$	$N_o = 4/q = 0.75$	$N_r = 1/N_o = 2$	$N_r = 1/N_o = 4$	$N_r = 1/N_o = 4/q = 0.75$
512	2.77e-07	4.01e-04	1.52e-04	3.95e-04	6.27e-04	6.71e-04
1024	3.88e-07	1.52e-04	3.10e-05	1.62e-06	6.50e-04	4.53e-04
2048	6.71e-07	6.88e-05	6.37e-05	1.07e-07	5.92e-04	3.29e-04
4096	6.42e-07	3.21e-05	3.91e-06	1.10e-07	6.61e-04	7.48e-05
8192	6.54e-07	8.84e-06	2.90e-06	7.49e-08	8.52e-05	3.05e-05
16384	6.56e-07	3.39e-06	8.34e-07	8.74e-08	3.67e-05	1.03e-05

(B) Approximation of the standard deviation of the vertical velocity component $\sigma[v]$.

Samples	$N_o = 2$	$N_o = 4$	$N_o = 4/q = 0.75$	$N_r = 1/N_o = 2$	$N_r = 1/N_o = 4$	$N_r = 1/N_o = 4/q = 0.75$
512	2.13e-07	1.50e-04	7.32e-05	5.37e-04	8.50e-04	9.09e-04
1024	1.98e-07	7.02e-05	2.32e-05	6.26e-07	8.81e-04	6.15e-04
2048	2.66e-07	4.72e-05	2.43e-05	5.98e-08	8.03e-04	1.33e-04
4096	2.36e-07	1.78e-05	5.72e-06	5.43e-08	2.53e-04	3.08e-05
8192	2.52e-07	5.07e-06	2.26e-06	3.96e-08	3.99e-05	1.41e-05
16384	2.61e-07	2.05e-06	6.99e-07	3.81e-08	1.44e-05	4.49e-06

increases) outperform other surrogate models in accuracy. However, the accuracy of other surrogate models also increases with the increasing number of training samples.

4.1.3. GSA using Sobol' indices

As we have seen in the previous section, aMR-PC with $N_r = 1$, $N_o = 2$ demonstrates the best performance in terms of accuracy. Therefore, we focus on this surrogate model for the GSA of the uncertain parameters. To assess the reliability of the estimated sensitivity indices, we examine how the space-averaged total sensitivity

indices, covering the entire spatial domain, change as the number of training samples increases, as shown in Fig 10, 11. To avoid the influence of physically not meaningful results, we excluded the low variance $\sigma^2 < 10^{-10}$ from the evaluation. In all considered test series, we can observe that a reasonable approach of the final values was achieved with 2048 training samples. Changes in total sensitivity indices calculated from the expansion coefficients of the aMR-PC surrogate models obtained from more than 4096 training samples are only minimal. Moreover, when we compare the total sensitivity indices shown in Tab. 6 with the Sobol' sensitivity indices in Tab. 7, 8, we notice that the trends in results derived from aPC with $N_o = 2$ are similar. Consequently, these trends indirectly validate the findings derived from the aMR-PC surrogate model with $N_r = 1$, $N_o = 2$. Hyperbolic truncation affects not only intermediate Sobol' terms but also the total indices computed from truncated expansions, leading to unreliable behavior.

In this work, we compute first-order and total-effect Sobol' indices to quantify the influence of individual parameters and their interactions on the surrogate outputs. The distributions of the total Sobol' indices, computed using aMR-PC with $N_r = 1$, $N_o = 2$ on 8192 samples, for the horizontal velocity u and the vertical velocity v in the filtration problem (Case 1) are shown in Fig. 8 and 9, respectively. Here, the total Sobol' indices of both velocity components are presented for uncertain stress jump parameter β_{sj} ($I = 1$), permeability in the complex interface k_Γ ($I = 2$), effective viscosity μ_{eff} ($I = 3$), the Beavers–Joseph parameter α_{BJ} ($I = 4$) and porous-medium permeability k_{pm} ($I = 5$).

In Fig. 8 and 9, we observe that both velocity components exhibit highly nonlinear behavior in response to variations in all five uncertain parameters. In particular, sharp fronts can be observed in the middle of the free-flow subdomain. This nonlinearity arises from the boundary conditions of the filtration problem. The stress jump parameter β_{sj} and the permeability in the complex interface k_Γ significantly influence both velocity components in the entire flow domain (Fig. 8(A,B), Fig. 9(A,B)). These two parameters appear in the stress jump terms between the free-flow domain and the complex interface Γ (see (2.8)–(2.11)). In the filtration problem, the flow is driven from the porous-medium region into the free-flow domain, therefore the velocities in these two flow regions are comparable (Fig. 3, right). The coupled model is sensitive to variations in the stress jump parameter and the permeability in the complex interface in both subdomains. In contrast, as we will see in Case 2 later, different behavior arises when the velocity in the free-flow region is much higher than in the porous medium.

Figures 8(C) and 9(C) indicate that the effective viscosity μ_{eff} mainly affects the flow in the free-flow domain. Although μ_{eff} appears in the higher-order correction terms of the averaged Brinkman equations (2.8), (2.9) and in the transmission conditions (2.10)–(2.12), its impact on the porous-medium region remains small. The Beavers–Joseph parameter α_{BJ} has the smallest effect among the parameters considered (Fig. 8(D), 9(D)), as it mainly reflects the interface roughness at the bottom of the transition region. Compared to the porous-medium region, the flow in the free-flow domain is slightly more sensitive to variations in the parameter α_{BJ} . Figures 8(E) and 9(E) show that both velocity components in the porous medium are very sensitive to changes in the porous-medium permeability k_{pm} , as it appears in Darcy's law (2.5) and directly controls the velocity magnitude in the porous-medium region. These findings are consistent with the results presented in [28], where the GSA was performed for the classical Stokes–Darcy model.

We note that both Sobol' indices and total sensitivity indices are normalized by the variance (Fig. 6(E,F)). Consequently, numerical errors may be amplified in regions where the variance is close to zero, as illustrated by the sharp fronts in the porous-medium region in Fig. 8(E) and 9(E). The results in such regions are therefore not necessarily meaningful from a modeling perspective.

To obtain a compact representation of the parameter influence, we employ space-averaged Sobol' sensitivity indices, which provide a global measure of parameter effects in the flow domain. Figures 10 and 11 display box plots and mean bar plots of the Sobol' indices for five uncertain parameters across different sample sizes ranging from 512 to 16,384. Convergence of the Sobol' sensitivity indices with respect to the number of samples is evident for both velocity components (see box plots and histograms in Fig. 10 and 11). From 2048 samples onward, both the distributions and the averaged values exhibit stable behavior. We therefore select 8192 samples as a representative case and present the corresponding box plots of the Sobol' indices together

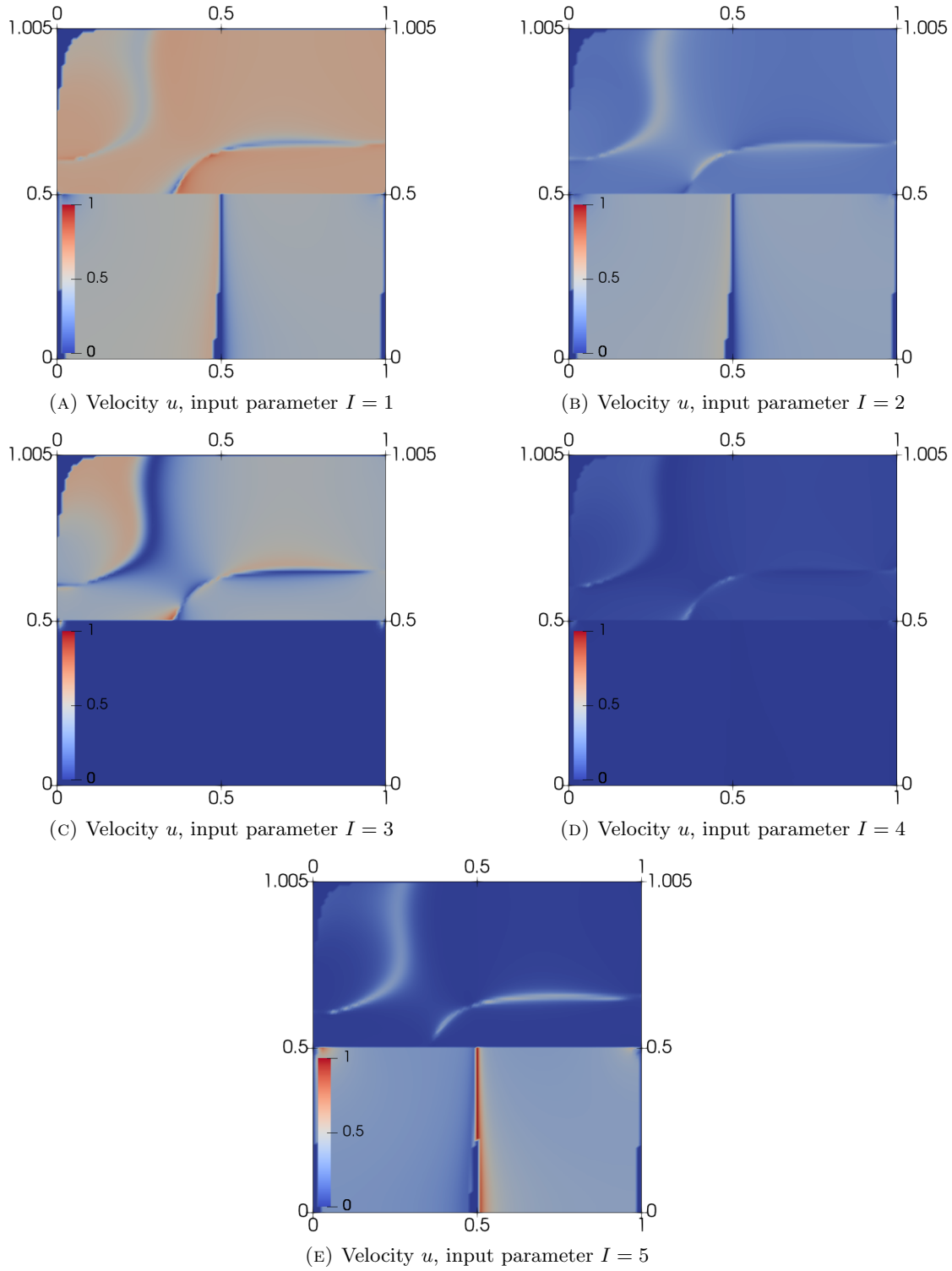


FIGURE 8. Case 1: Total Sobol' indices of the horizontal velocity u obtained from aMR-PC-surrogate with $N_r = 1, N_o = 2$, trained on 8192 QMC samples.

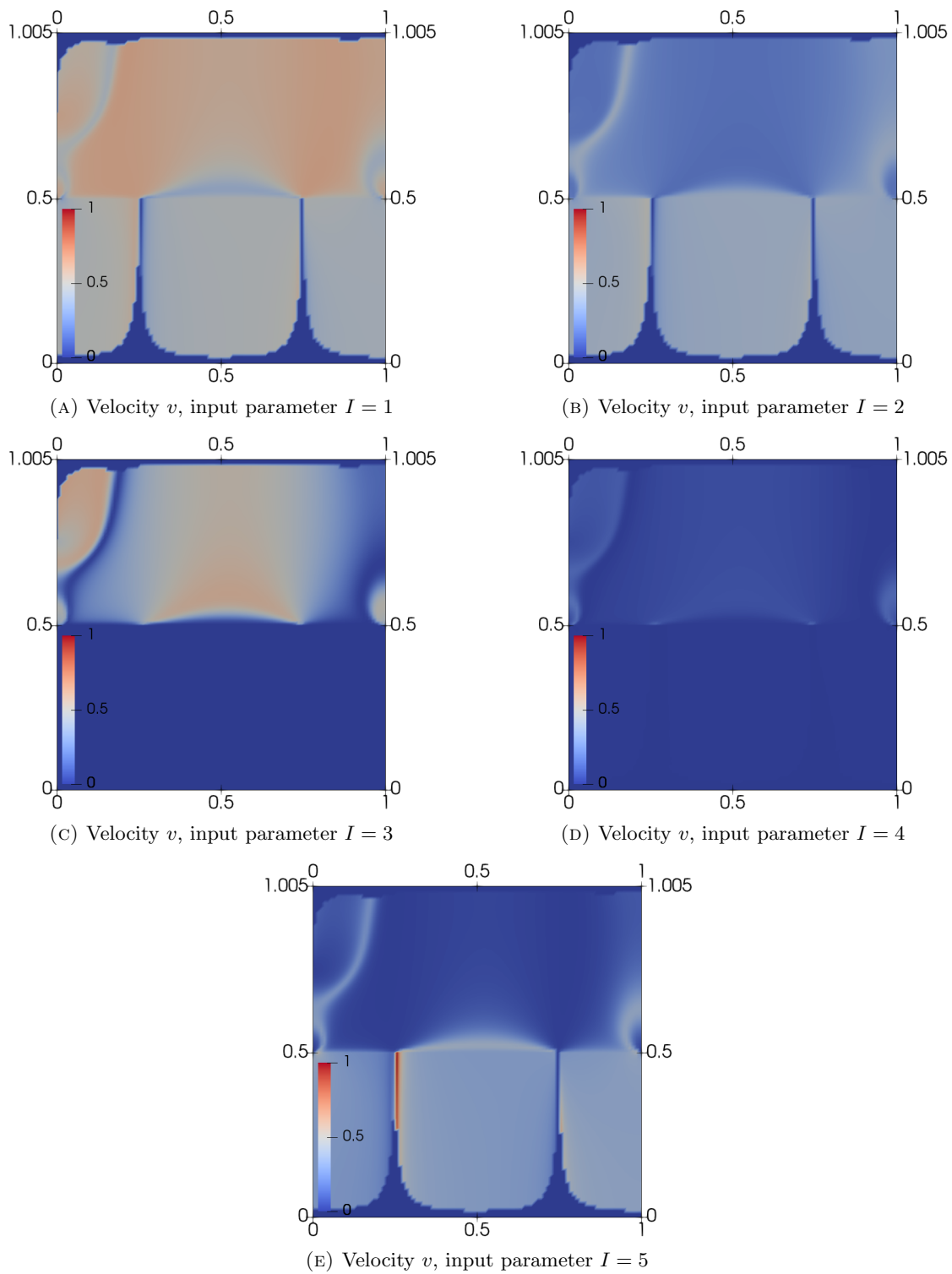


FIGURE 9. Case 1: Total Sobol' indices of the vertical velocity v obtained from aMR-PC-surrogate with $N_r = 1, N_o = 2$, trained on 8192 QMC samples.

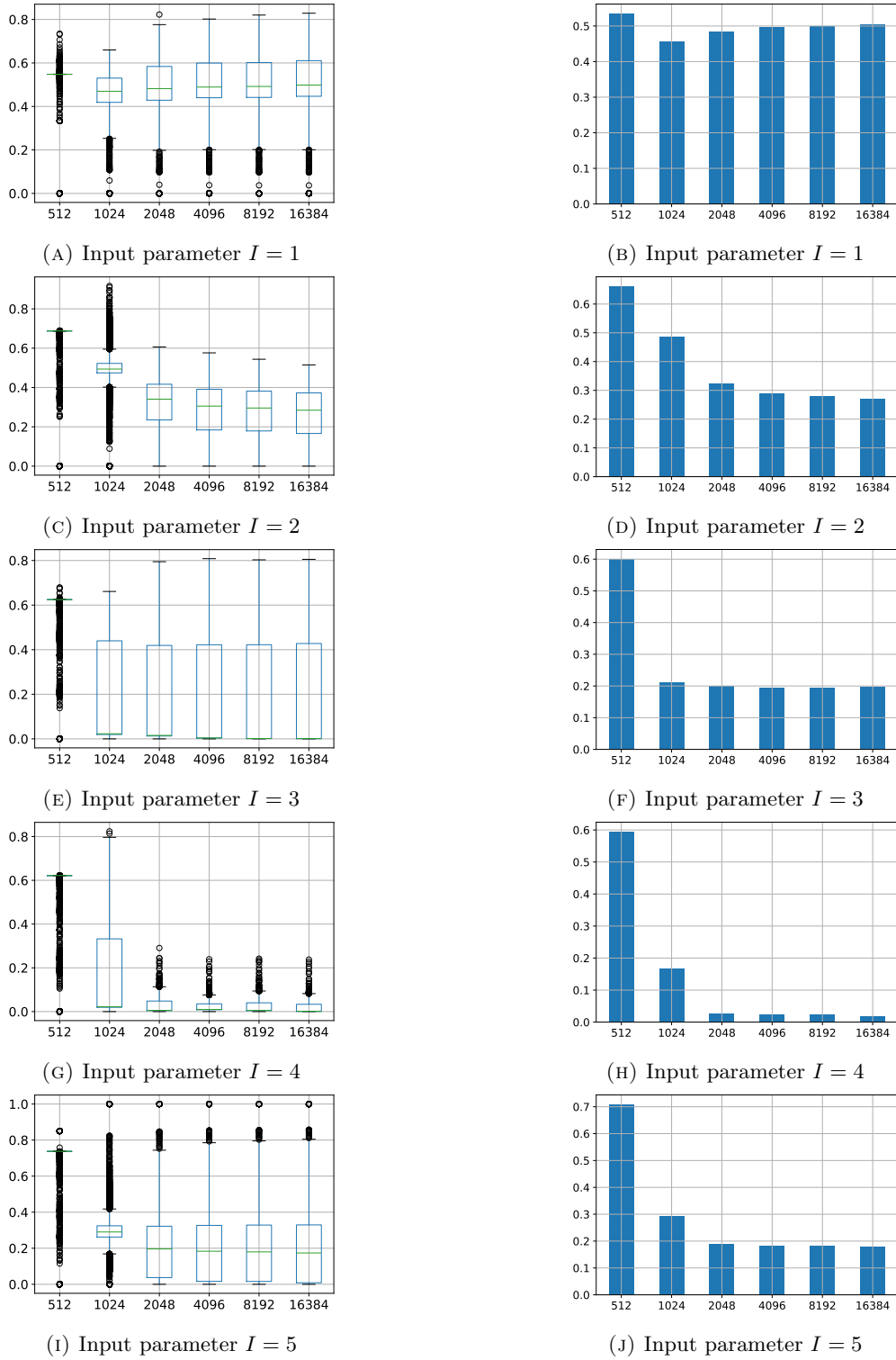


FIGURE 10. Case 1: Evolution of the total sensitivity indices of the horizontal velocity u obtained from aMR-PC-surrogate with $N_r = 1$, $N_o = 2$.

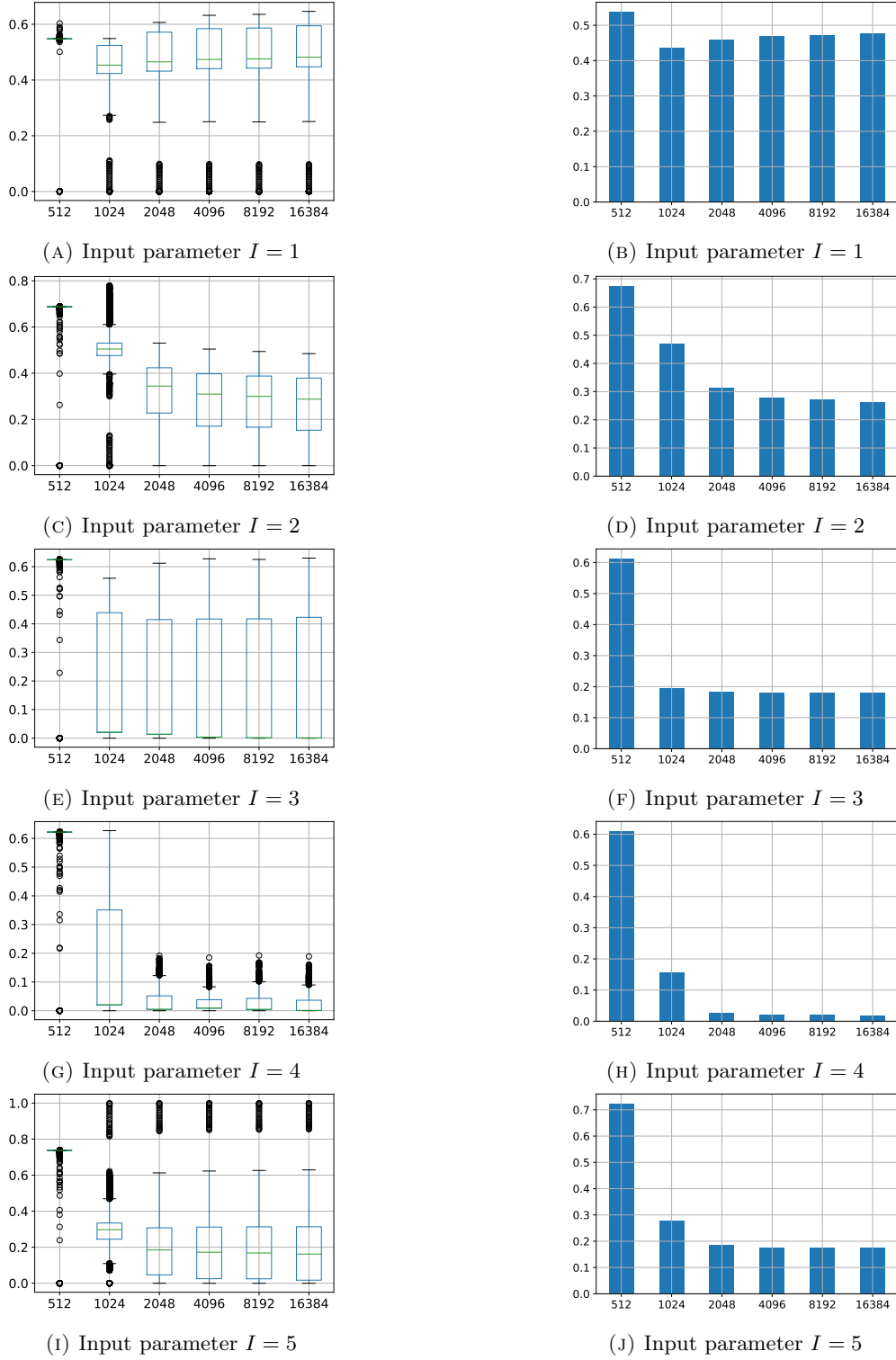


FIGURE 11. Case 1: Evolution of the total sensitivity indices of the vertical velocity v obtained from aMR-PC-surrogate with $N_r = 1$, $N_o = 2$.

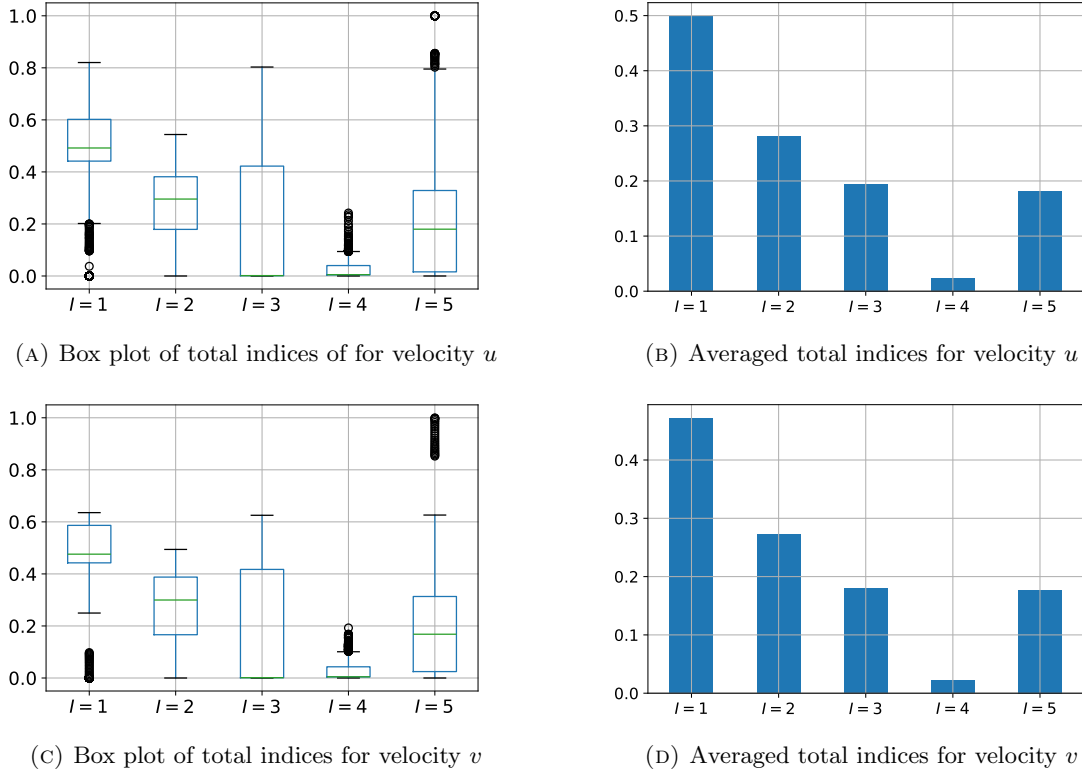


FIGURE 12. Case 1: Evaluation of the total sensitivity indices over the whole domain, obtained from aMR-PC-surrogate with $N_r = 1$, $N_o = 2$, trained on 8192 QMC samples.

with histograms of their averaged values in Fig. 12. The results reveal that, within the framework of the newly derived hybrid-dimensional Stokes–Brinkman–Darcy model, the flow model is most sensitive to the stress jump parameter β_{sj} (Fig. 12(B,D)). The permeability of the complex interface k_Γ and the porous-medium permeability k_{pm} have also significant influence. The box plot of the effective viscosity μ_{eff} shows relatively low median values (Fig. 12(A,C)). Nevertheless, the averaged Sobol’ index indicates significant influence of μ_{eff} , which can be explained by its primary impact in the free-flow domain. The Beavers–Joseph parameter α_{BJ} shows only minor impact in this test case, although its box plot variability indicates occasional strong contributions in specific realizations (outliers).

4.2. Case 2: Postprocessing and evaluation

We next proceed with the second test case introduced in Section 2.5, which describes the splitting flow problem. In this setting, the flow enters and exits through the boundary of the free-flow domain, resulting in significantly higher velocities in the free-flow region compared to the porous medium. The permeability of the porous medium controls the amount of fluid that can pass through the complex interface. Based on the experience gained from Case 1, we omit the evaluations of the aMR-PC surrogate models for $N_r = 1$, $N_o = 4$, both with and without hyperbolic truncation-based sparsity.

4.2.1. Mean and variance

We visualize the mean, standard deviation, and log-variance obtained from the aMR-PC expansion with polynomial degree $N_o = 2$ and refinement level $N_r = 1$ in Fig. 13. The comparison with MC results using 50,000 samples is omitted here, since the aMR-PC expansion reproduces the MC statistics with high fidelity. The

TABLE 4. Case 2: L^2 -error of the approximation of the mean (\mathbb{E}).(A) Approximation of the mean of the horizontal velocity component $\mathbb{E}[u]$.

Samples	$N_o = 2$	$N_o = 4$	$N_o = 4/q = 0.75$	$N_r = 1/N_o = 2$
512	5.10e-06	1.53e-04	5.21e-05	4.01e-03
1024	2.12e-06	5.35e-05	8.60e-06	3.70e-06
2048	4.95e-07	1.94e-05	2.07e-05	1.84e-06
4096	2.69e-07	9.00e-06	1.34e-06	9.98e-07
8192	4.56e-07	2.05e-06	7.32e-07	3.56e-07
16384	4.41e-07	7.86e-07	4.56e-08	1.72e-07

(B) Approximation of the mean of the vertical velocity component $\mathbb{E}[v]$.

Samples	$N_o = 2$	$N_o = 4$	$N_o = 4/q = 0.75$	$N_r = 1/N_o = 2$
512	1.68e-06	5.04e-05	1.72e-05	3.11e-03
1024	6.92e-07	1.77e-05	2.82e-06	1.21e-06
2048	1.59e-07	6.42e-06	6.83e-06	6.04e-07
4096	9.52e-08	2.98e-06	4.69e-07	3.26e-07
8192	1.56e-07	6.67e-07	2.44e-07	1.15e-07
16384	1.49e-07	2.55e-07	1.74e-08	6.03e-08

mean and variance in Fig. 13(A–D) further indicate that the velocity in the porous-medium region is relatively small, making the variance difficult to detect. The log-variance highlights the regions with comparatively larger relative fluctuations, making the small but non-negligible variability in the porous-medium region more visible (Fig. 13(E, F)).

4.2.2. Accuracy of the approximation

As in the previous test case, we start with the assessment of the accuracy in terms of RMSE and relative MSE shown in Fig. 14. Also in this case, errors are computed over the spatial domain using 10,000 randomly selected test parameter sets not used for training. Here, aPC with $N_o = 2$ provides the best accuracy using 512 training samples. However, the improvement for increasing number of training samples is only minimal. We observe that aMR-PC with $N_r = 1$, $N_o = 2$ outperforms all other surrogate models in terms of accuracy if more than 1024 samples are used for training.

Evaluation of the L^2 -error of the approximation of the mean using Eq. (3.4) in comparison with the MC result computed with 50,000 samples is provided in Tab. 4. It demonstrates a similar final precision for all surrogates. Again, aPC with $N_o = 2$ shows a better accuracy for lower numbers of training samples. Evaluating the L^2 -error in approximation of the standard deviation using Eq. (3.5) against the MC reference solution computed using 50,000 samples, as presented in Tab. 5, reveals that aPC with $N_o = 2$ offers optimal accuracy with fewer training samples, while aMR-PC with $N_r = 1$, $N_o = 2$ provides the best precision when using a larger number of training samples.

4.2.3. GSA using Sobol' indices

Also in this test case, the aMR-PC-based surrogate with $N_r = 1$, $N_o = 2$ demonstrates a superior accuracy performance. Therefore, this surrogate is used for the GSA in this section. Analyzing the convergence behavior of the averaged total sensitivity indices presented in Fig. 15 and Fig. 16 for the velocity components u and v , respectively, we observe only minimal changes after 4096 training samples. By examining the total sensitivity indices presented in Tab. 9 along with the Sobol' sensitivity indices shown in Tab. 10 and Tab. 11 for u and v , respectively, it is evident that the outcomes derived from the expansion coefficients of the aPC-based surrogate model with $N_o = 2$ align with the results computed using aMR-PC with $N_r = 1$, $N_o = 2$. This alignment serves

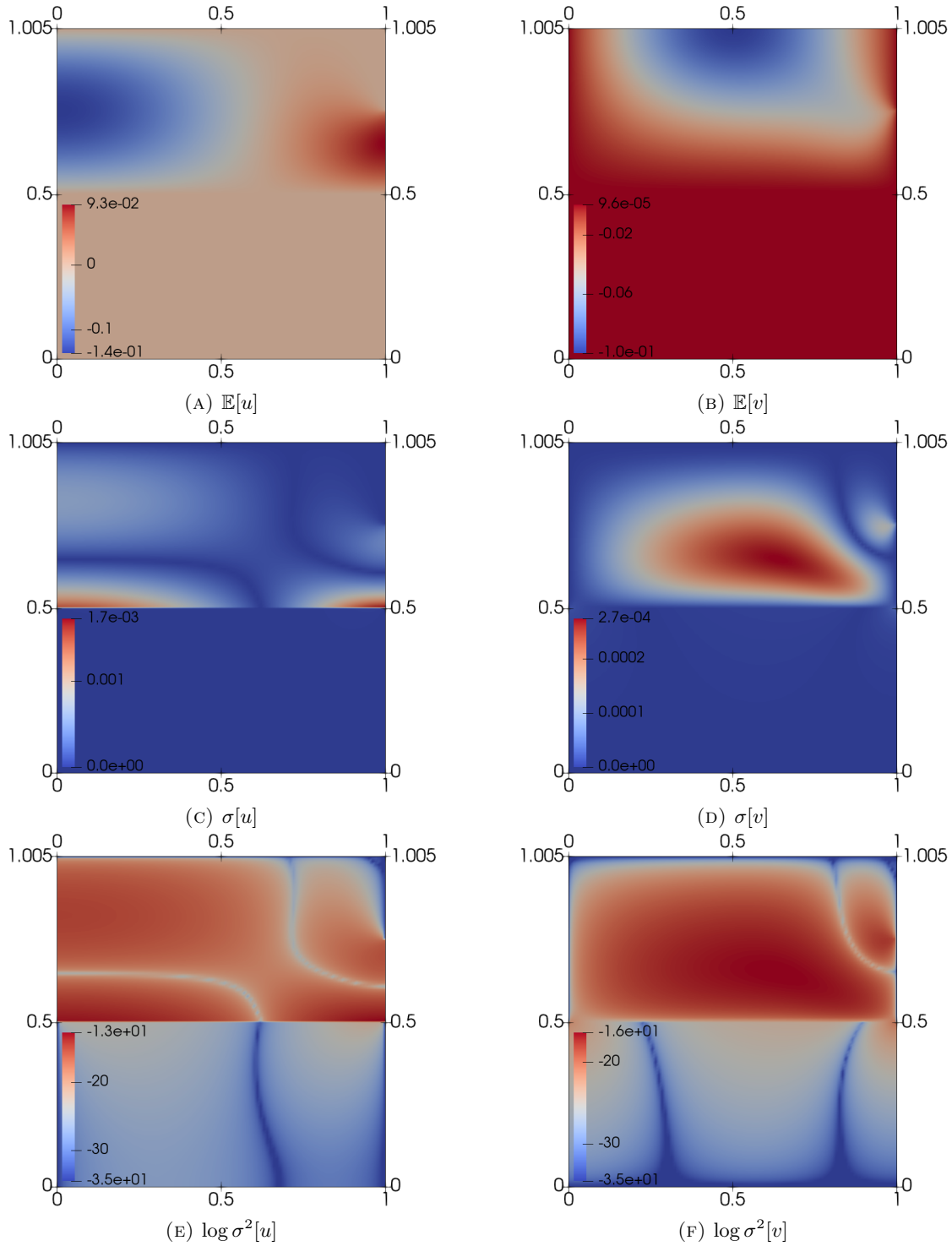
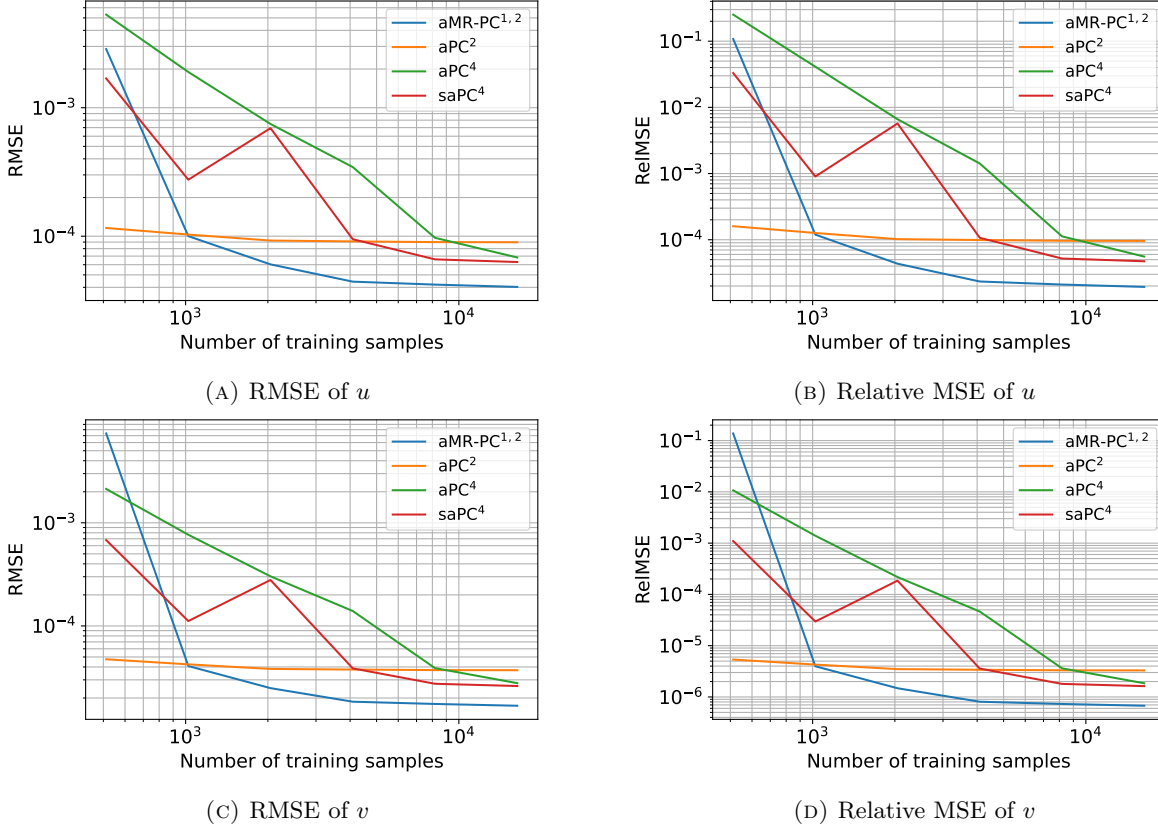


FIGURE 13. Case 2: Mean, standard deviation and log-variance of the horizontal and vertical velocities (u, v) obtained from aMR-PC-surrogate with $N_r = 1, N_o = 2$, trained on 8192 QMC samples.

FIGURE 14. Case 2: RMSE and relative MSE error plots for 512, \dots , 16384 training samples.TABLE 5. Case 2: L^2 -error of the approximation of the standard deviation σ .(A) Approximation of the standard deviation of the horizontal velocity component $\sigma[u]$.

Samples	$N_o = 2$	$N_o = 4$	$N_o = 4/q = 0.75$	$N_r = 1/N_o = 2$
512	8.58e-06	1.50e-02	5.55e-03	1.21e-02
1024	1.32e-05	5.59e-03	9.61e-04	6.73e-05
2048	2.45e-05	2.35e-03	2.35e-03	4.93e-06
4096	2.34e-05	1.12e-03	1.70e-05	3.06e-06
8192	2.39e-05	3.09e-04	8.77e-05	1.66e-06
16384	2.39e-05	1.17e-04	2.55e-05	2.21e-06

(B) Approximation of the standard deviation of the vertical velocity component $\sigma[v]$.

Samples	$N_o = 2$	$N_o = 4$	$N_o = 4/q = 0.75$	$N_r = 1/N_o = 2$
512	2.90e-06	4.95e-03	1.83e-03	9.45e-03
1024	4.38e-06	1.85e-03	3.16e-04	2.26e-05
2048	8.11e-06	7.78e-04	7.77e-04	1.62e-06
4096	7.73e-06	3.72e-04	7.24e-06	1.04e-06
8192	7.92e-06	1.01e-04	2.96e-05	5.59e-07
16384	7.93e-06	3.84e-05	8.43e-06	7.41e-07

as an indirect confirmation of these findings. As in Case 1, hyperbolic truncation yields unreliable indices when computed from truncated expansion coefficients.

We again compute first-order and total-effect Sobol' indices (parameters as in Tab. 1) to quantify individual and interaction effects for the splitting flow problem. The space distribution of the total Sobol' indices of both velocity components u and v , computed using aMR-PC with $N_r = 1$, $N_o = 2$ with 8192 samples, are visualized in Fig. 15 and Fig.16. These results reveal that both velocity components exhibit highly nonlinear behavior with respect to variations in all five uncertain parameters in the splitting flow problem. In particular, sharp fronts emerge in both the free-flow and porous-medium regions. This nonlinearity is attributed to the specific boundary conditions imposed in the splitting flow problem.

The stress jump parameter β_{sj} and the permeability in the complex interface k_Γ predominantly influence both velocity components in the free-flow domain (Fig. 15(A,B), Fig. 16(A,B)). In the splitting flow problem, the flow is driven and exits through the free-flow region, where the velocities are considerably larger than in the porous-medium regions (Fig. 4, right). As a result, the flow in the free-flow subdomain is particularly sensitive to changes in the stress jump parameter and the interface permeability. Figures 15(C) and 16(C) indicate that the effective viscosity μ_{eff} mainly affects the free-flow domain as in the filtration problem in Section 4.1.3.

The Beavers–Joseph parameter α_{BJ} has a comparatively smaller effect than the other parameters, with most variations concentrated along the complex interface (Fig. 15(D), Fig. 16(D)). This behavior reflects the role of α_{BJ} in characterizing the interface roughness at the bottom of the transition region. As can be seen from Fig. 15(E) and Fig. 16(E), both velocity components in the porous medium are particularly sensitive to variations in the porous-medium permeability k_{pm} . This is expected, since the relatively small porous-medium permeability directly controls how much flow can enter the porous region through the complex interface, consistent with [28].

We note again that both the Sobol' indices and total Sobol' indices are normalized by variance (Fig. 13(E, F)). As a consequence, numerical errors can be amplified in regions where the variance is close to zero. Hence, the results in these regions are not necessarily meaningful from a modeling perspective.

Figures 17, 18 display the box plots (left) and the mean bar plots (right) of the Sobol' indices for five uncertain parameters across different sample sizes ranging from 512 to 16384 in the splitting flow problem. Convergence of the Sobol' sensitivity indices with respect to the number of samples is evident in both the box plots and the averaged indices. From 2048 samples onward, both the distributions and the averaged values exhibit stable behavior (Fig. 17, 18).

We therefore select 8192 samples as a representative case and present the corresponding box plots of the Sobol' indices together with histograms of their space-averaged values in Fig. 19. Compared to the filtration problem (Fig. 12(A,C)), the medians of the total indices are smaller across all uncertain parameters (Fig. 19(A,C)). This can be explained by the fact that the influence of the parameters is primarily concentrated in one of the subdomains (Fig. 15, 16). These results reveal that the newly derived hybrid-dimensional Stokes–Brinkman–Darcy model for the splitting flow problem is most sensitive to the porous-medium permeability k_{pm} (Fig. 19(B,D)). The stress jump parameter β_{sj} and the effective viscosity μ_{eff} also have significant influence. In contrast, the Beavers–Joseph parameter α_{BJ} shows only minor impact and is not essential in this test case, although its box plot variability indicates occasional strong contributions in specific realizations (outliers), consistent with the previous findings for the filtration problem (Case 1).

5. CONCLUSIONS

In the current study, we evaluated the appropriateness of various non-regularized PCE-based surrogate models for GSA when training samples are provided through a space-filling Sobol' sequence. This scenario is particularly relevant if the training data cannot be generated on demand and are instead provided by observation. However, we find that surrogates with maximum polynomial degree $N_o = 2$ yield reliable GSA results. In particular, aMR-PC with $N_r = 1$, $N_o = 2$ achieves the highest accuracy in the comparison, since a sufficient quantity of training samples was available, making it the preferred choice for conducting GSA of the Stokes–Brinkman–Darcy flow model.

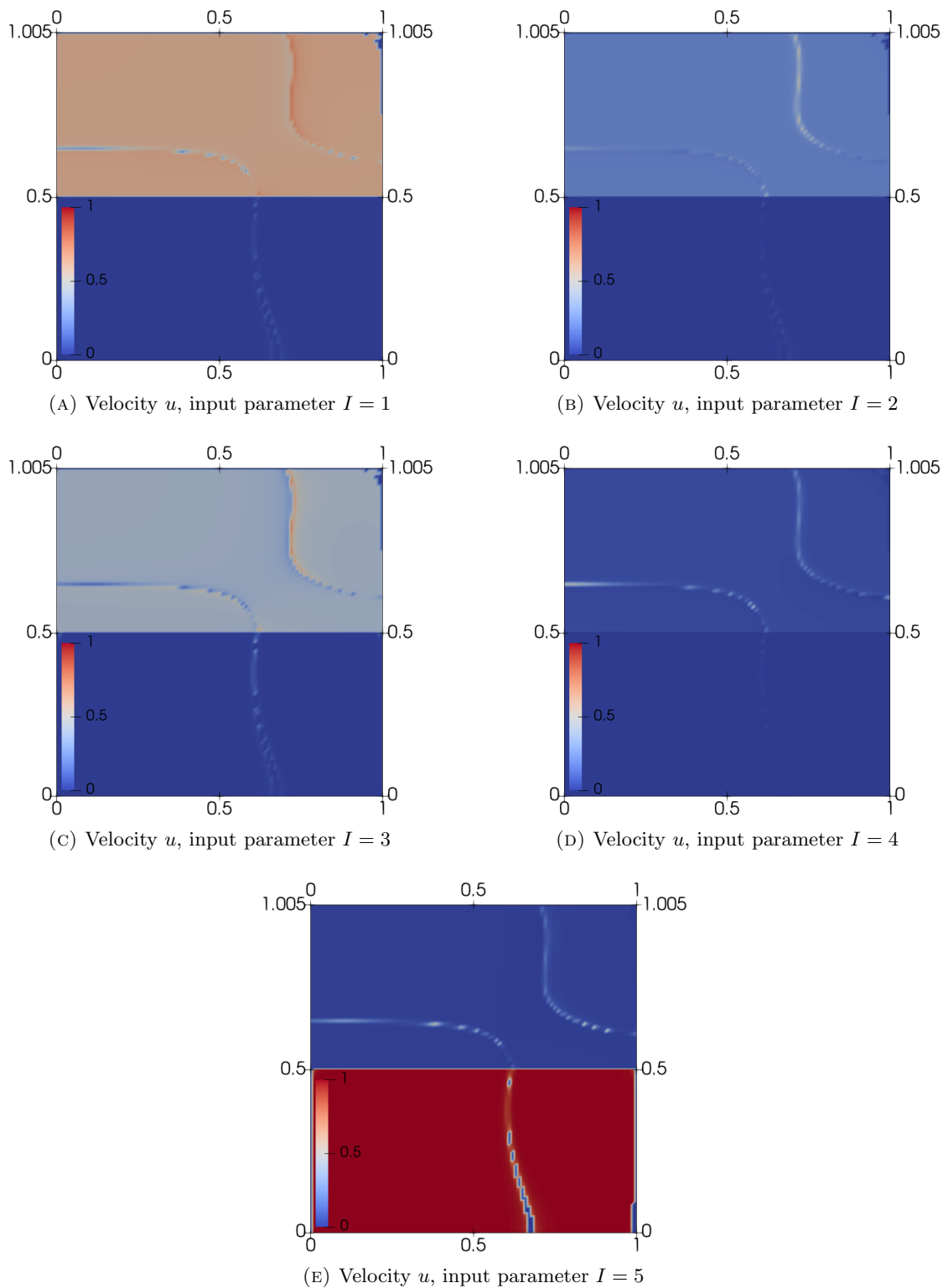


FIGURE 15. Case 2: Total sensitivity indices of the horizontal velocity u obtained from aMR-PC-surrogate with $N_r = 1, N_o = 2$, trained on 8192 QMC samples.

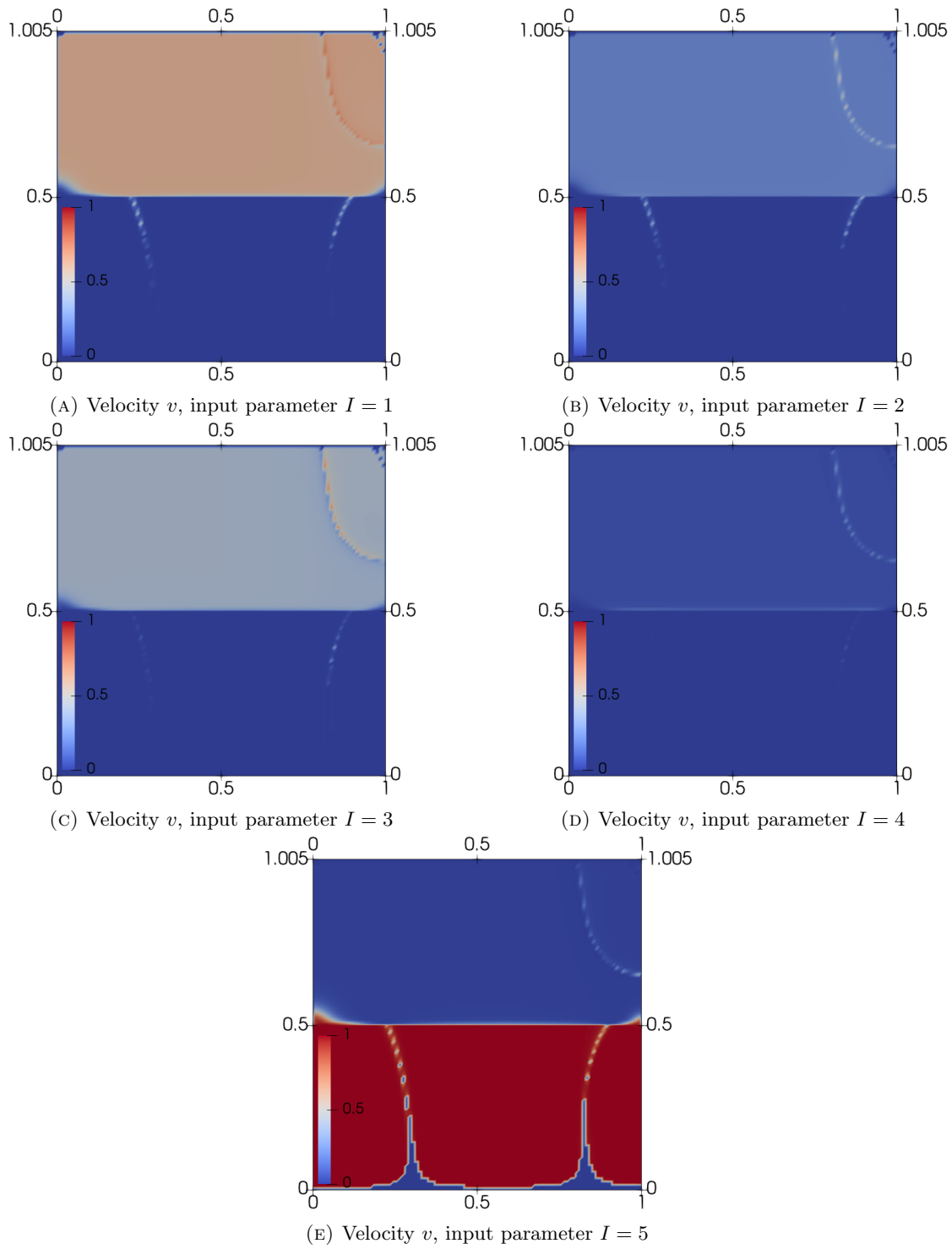


FIGURE 16. Case 2: Total sensitivity indices of the vertical velocity v obtained from aMR-PC-surrogate with $N_r = 1, N_o = 2$, trained on 8192 QMC samples.

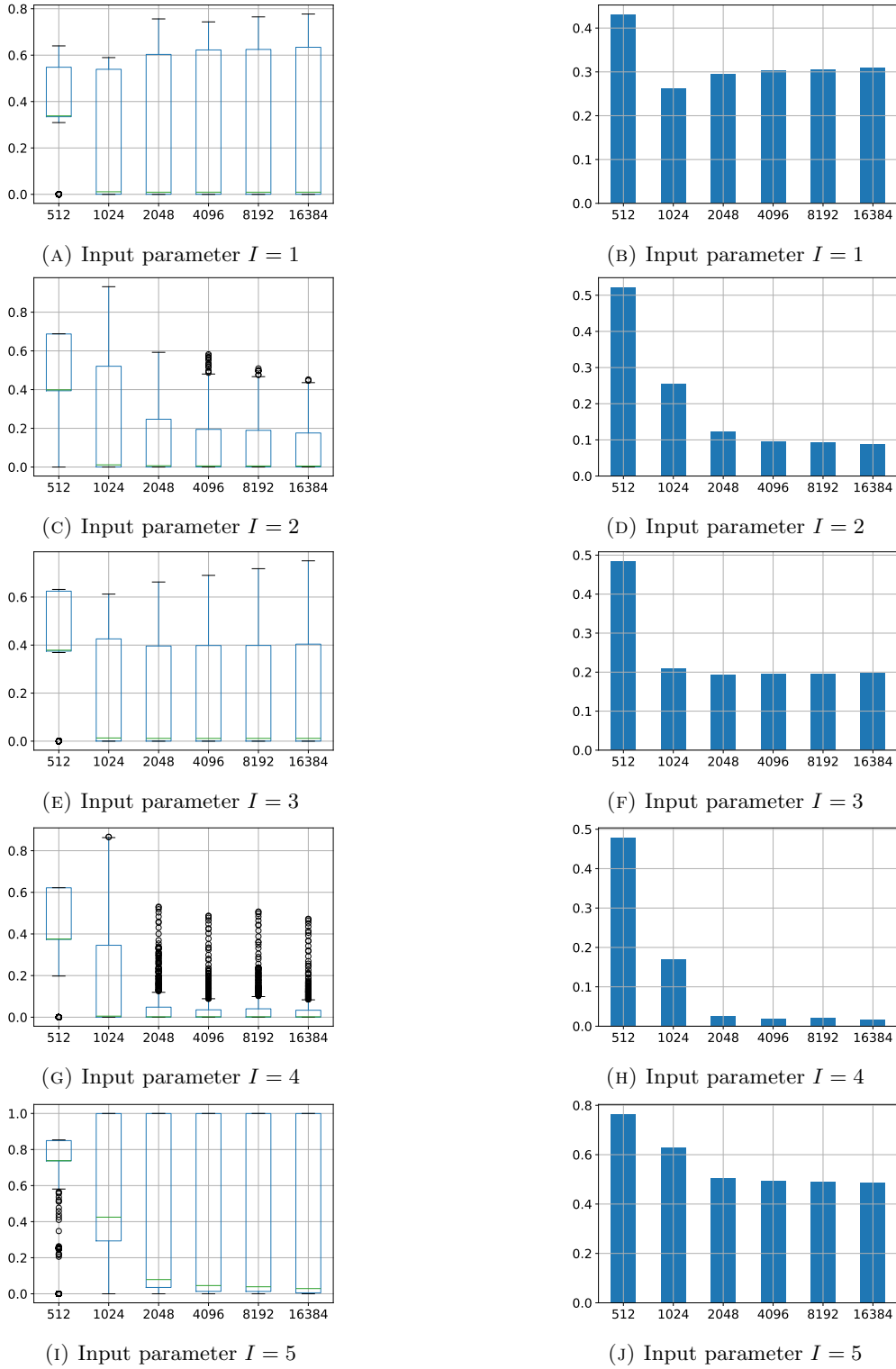


FIGURE 17. Case 2: Evolution of the total sensitivity indices of the horizontal velocity u obtained from aMR-PC-surrogate with $N_r = 1$, $N_o = 2$.

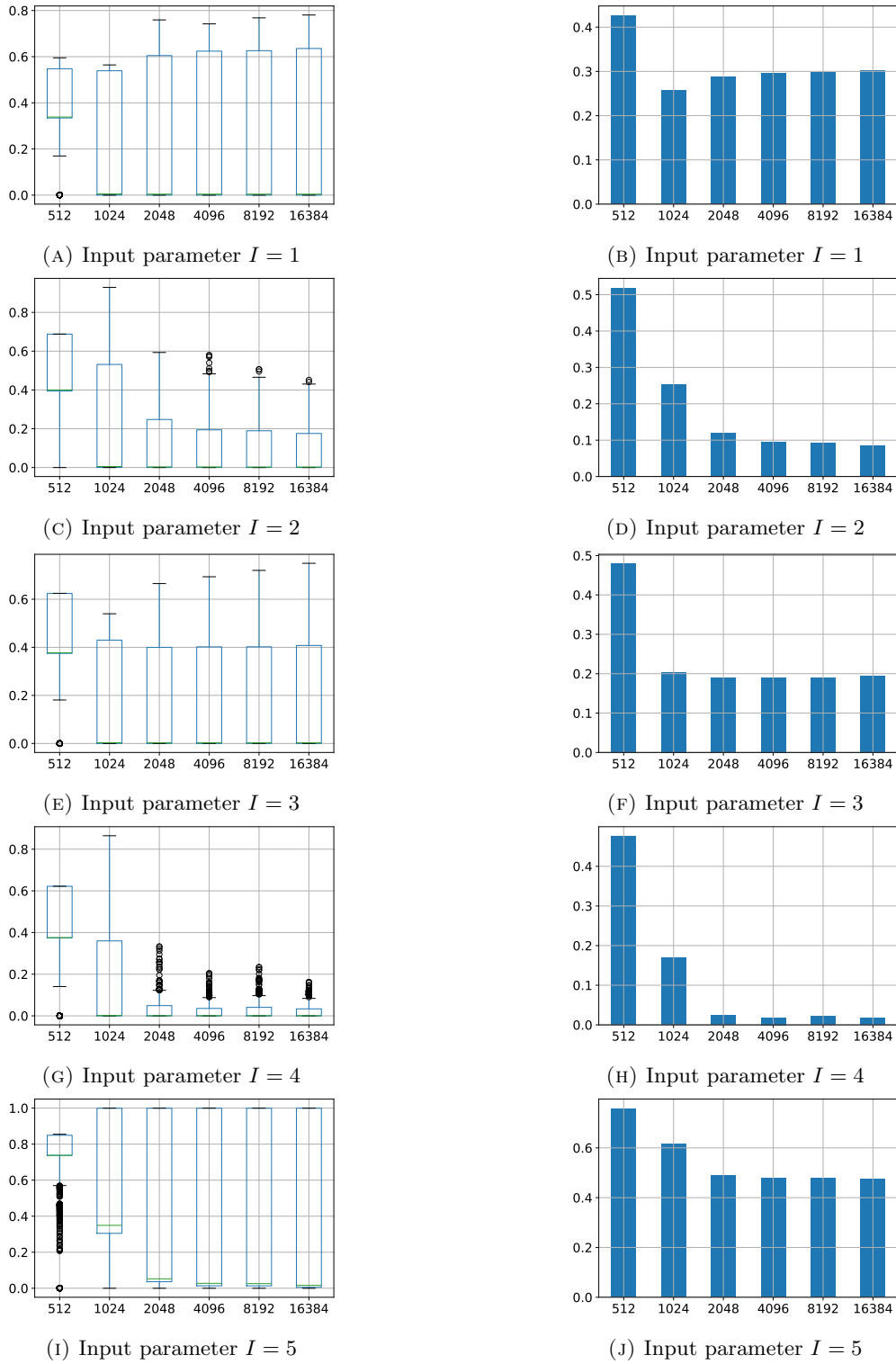


FIGURE 18. Case 2: Evolution of the total sensitivity indices of the vertical velocity v obtained from aMR-PC-surrogate with $N_r = 1$, $N_o = 2$.

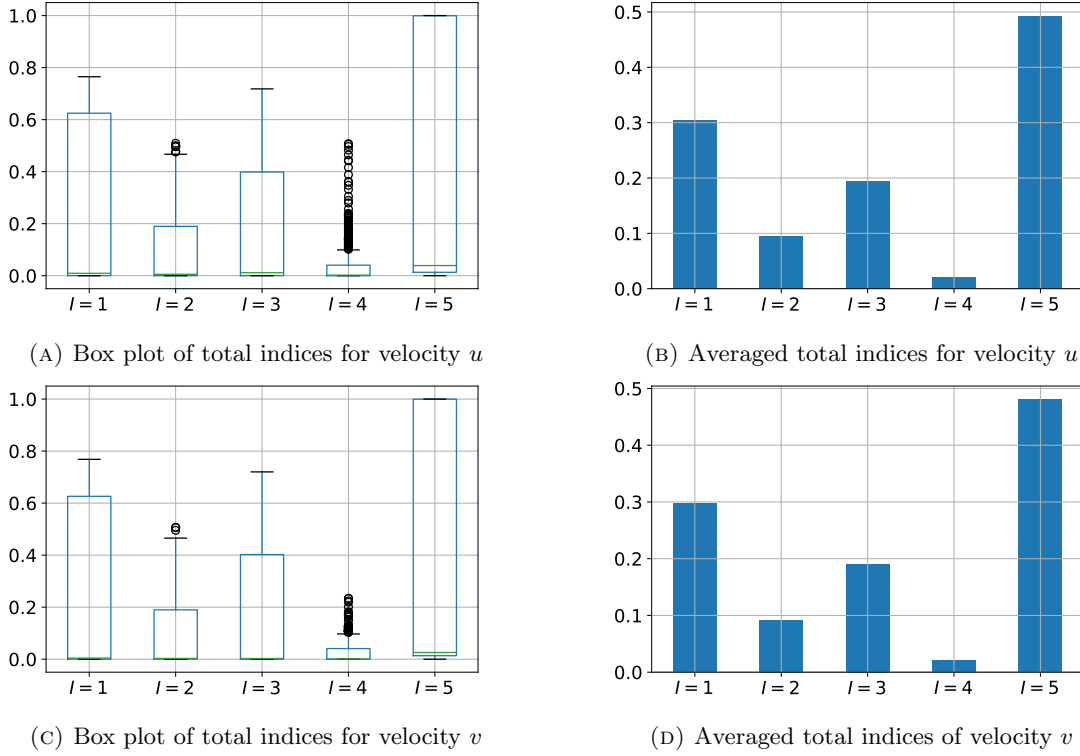


FIGURE 19. Case 2: Evaluation of the total sensitivity indices over the whole domain, obtained from aMR-PC-surrogate with $N_r = 1, N_o = 2$, trained on 8192 QMC samples.

In this work, two test cases have been investigated for GSA: a filtration problem and a splitting flow problem. Analyzing the total sensitivity indices, we observed that the aMR-PC surrogate of the Stokes–Brinkman–Darcy flow model is highly sensitive to the stress jump parameter, the permeability of the complex interface, the effective viscosity, and the porous-medium permeability in both test cases. For the filtration problem (Case 1), the stress jump parameter has the most significant influence, whereas for the splitting flow problem (Case 2), the porous-medium permeability is the dominant factor.

In both cases, the Beavers–Joseph coefficient does not significantly affect the overall flow behavior, but it influences the fluid behavior locally near the complex interface. The porous-medium permeability, within the considered parameter range, has no strong influence on the free-flow velocity. The influence of the Beavers–Joseph coefficient and the porous-medium permeability is consistent with the results reported in [28]. The effective viscosity primarily impacts the free-flow region rather than the porous-medium region in both test cases. The sensitivity to the stress jump parameter and the interface permeability depends on the specific test case. In the filtration problem (Case 1), where the fluid velocities in the free-flow and porous-medium regions are comparable, the entire flow domain is highly sensitive to both parameters. In contrast, in the splitting flow problem (Case 2), where the free-flow velocity is relatively higher, both parameters are influential only in the free-flow region.

Several directions remain open for future research. One possible extension of this work is to consider finer mesh resolutions. Although finer meshes would improve the accuracy of the reference solutions, they would also increase the computational effort. Since the present study serves as a benchmark for surrogate models, the insights obtained here can guide future reductions in the number of required training samples and the set of surrogate configurations to compare. Another natural direction is to incorporate a larger set of input parameters

in GSA, for instance by accounting for anisotropic porous media. In this case, the stress jump tensor β as well as the permeability tensors \mathbf{K}_Γ and \mathbf{K}_{pm} would be treated as fully anisotropic. Such an extension would allow for a more comprehensive characterization of uncertainties in the hybrid-dimensional Stokes–Brinkman–Darcy flow model and, at the same time, open opportunities for developing and testing advanced surrogate strategies capable of efficiently handling the expanded parameter space.

Data Availability Statement

The research data associated with this article are available in DaRUS [47].

REFERENCES

- [1] P. Angot, B. Goyeau, and J. A. Ochoa-Tapia. Asymptotic modeling of transport phenomena at the interface between a fluid and a porous layer: jump conditions. *Phys. Rev. E*, 95(6):063302, 2017.
- [2] P. Angot, B. Goyeau, and J. A. Ochoa-Tapia. A nonlinear asymptotic model for the inertial flow at a fluid-porous interface. *Adv. Water Res.*, 149:103798, 2021.
- [3] R. Askey and J. Wilson. Some basic hypergeometric orthogonal polynomials that generalize Jacobi polynomials. *Mem. Amer. Math. Soc.*, 54(319):iv+55, 1985.
- [4] G. S. Beavers and D. D. Joseph. Boundary conditions at a naturally permeable wall. *J. Fluid Mech.*, 30:197–207, 1967.
- [5] G. Blatman and B. Sudret. Efficient computation of global sensitivity indices using sparse polynomial chaos expansions. *Reliab. Eng. Syst. Saf.*, 95(11):1216–1229, 2010.
- [6] G. Blatman and B. Sudret. Adaptive sparse polynomial chaos expansion based on least angle regression. *J. Comput. Phys.*, 230(6):2345–2367, 2011.
- [7] R. Bürger, I. Kröker, and C. Rohde. A hybrid stochastic Galerkin method for uncertainty quantification applied to a conservation law modelling a clarifier-thickener unit. *ZAMM Z. Angew. Math. Mech.*, 94(10):793–817, 2014.
- [8] P.-C. Bürkner, I. Kröker, S. Oladyshkin, and W. Nowak. A fully Bayesian sparse polynomial chaos expansion approach with joint priors on the coefficients and global selection of terms. *J. Comput. Phys.*, page 112210, 2023.
- [9] S. Da Veiga, F. Gamboa, B. Iooss, and C. Prieur. *Basics and trends in sensitivity analysis—theory and practice in R*, volume 23 of *Computational Science & Engineering*. Society for Industrial and Applied Mathematics (SIAM), Philadelphia, PA, 2021.
- [10] M. Discacciati, E. Miglio, and A. Quarteroni. Mathematical and numerical models for coupling surface and groundwater flows. *Appl. Num. Math.*, 43:57–74, 2002.
- [11] M. Discacciati and A. Quarteroni. Navier–Stokes/Darcy coupling: modeling, analysis, and numerical approximation. *Rev. Mat. Complut.*, 22:315–426, 2009.
- [12] J. Dréau, B. Magnain, and A. Batailly. Multi-element polynomial chaos expansion based on automatic discontinuity detection for nonlinear systems. *J. Sound Vib.*, 567:117920, 2023.
- [13] E. Eggenweiler and I. Rybak. Unsuitability of the Beavers–Joseph interface condition for filtration problems. *J. Fluid Mech.*, 892:A10, 2020.
- [14] E. Eggenweiler and I. Rybak. Effective coupling conditions for arbitrary flows in Stokes–Darcy systems. *Multiscale Model. Simul.*, 19:731–757, 2021.
- [15] O. G. Ernst, A. Mugler, H.-J. Starkloff, and E. Ullmann. On the convergence of generalized polynomial chaos expansions. *ESAIM Math. Model. Numer. Anal.*, 46(2):317–339, 2012.
- [16] J. Favard. Sur les polynomes de Tchebicheff. *CR Acad. Sci. Paris*, 200(2052-2055):11, 1935.
- [17] R. Fisher and W. Mackenzie. The manurial response of different potato varieties. *J. Agric. Sci.*, 13:311–320, 1923.
- [18] R. A. Fisher. Studies in crop variation. I. An examination of the yield of dressed grain from Broadbalk. *J. Agric. Sci.*, 11(2):107–135, 1921.
- [19] W. Gautschi. *Orthogonal Polynomials: Computation and Approximation*. Oxford University Press, New York, 2004.
- [20] R. G. Ghanem and P. D. Spanos. *Stochastic Finite Elements: a Spectral Approach*. Springer-Verlag, New York, 1991.
- [21] B. Goyeau, D. Lhuillier, D. Gobin, and M. Velarde. Momentum transport at a fluid–porous interface. *Int. J. Heat Mass Transfer*, 46:4071–4081, 2003.
- [22] T. Homma and A. Saltelli. Importance measures in global sensitivity analysis of nonlinear models. *Reliab. Eng. Syst. Saf.*, 52(1):1–17, 1996.
- [23] W. Jäger and A. Mikelić. Modeling effective interface laws for transport phenomena between an unconfined fluid and a porous medium using homogenization. *Transp. Porous Media*, 78:489–508, 2009.
- [24] J. Kang and M. Wang. Brinkman double-layer model for flow at a free-porous interface. *Int. J. Mech. Sci.*, 263:108770, 2024.
- [25] R. Kohlhaas, I. Kröker, S. Oladyshkin, and W. Nowak. Gaussian active learning on multi-resolution arbitrary polynomial chaos emulator: concept for bias correction, assessment of surrogate reliability and its application to the carbon dioxide benchmark. *Comput. Geosci.*, 27(3):1–21, 2023.

- [26] M. Köppel, I. Kröker, and C. Rohde. Intrusive uncertainty quantification for hyperbolic-elliptic systems governing two-phase flow in heterogeneous porous media. *Comput. Geosci.*, 21(4):807–832, 2017.
- [27] I. Kröker and S. Oladyshkin. Arbitrary multi-resolution multi-wavelet-based polynomial chaos expansion for data-driven uncertainty quantification. *Reliab. Eng. Syst. Saf.*, 222:108376, 2022.
- [28] I. Kröker, S. Oladyshkin, and I. Rybak. Global sensitivity analysis using multi-resolution polynomial chaos expansion for coupled Stokes–Darcy flow problems. *Comput. Geosci.*, 27:805–827, 2023.
- [29] I. Kröker, T. Brünnette, N. Wildt, M. F. M. Oreamuno, R. Kohlhaas, S. Oladyshkin, and W. Nowak. Bayesian³ active learning for regularized multi-resolution arbitrary polynomial chaos using information theory. *Int. J. Uncertain. Quantif.*, 15(3):21–54, 2025.
- [30] I. Kröker and S. Oladyshkin. aMR-PC: Arbitrary multi-resolution polynomial chaos python toolbox, 2023. <https://github.com/ikroeker/aMR-PC>.
- [31] J. Kusch, R. G. McClarren, and M. Frank. Filtered stochastic Galerkin methods for hyperbolic equations. *J. Comput. Phys.*, 403:109073, 2020.
- [32] U. Lācis and S. Bagheri. A framework for computing effective boundary conditions at the interface between free fluid and a porous medium. *J. Fluid Mech.*, 812:866–889, 2017.
- [33] U. Lācis, Y. Sudhakar, S. Pasche, and S. Bagheri. Transfer of mass and momentum at rough and porous surfaces. *J. Fluid Mech.*, 884:A21, 2020.
- [34] D. Lasseux, F. J. Valdés-Parada, and A. Bottaro. Upscaled model for unsteady slip flow in porous media. *J. Fluid Mech.*, 923:A37, 2021.
- [35] O. P. Le Maître, H. N. Najm, R. G. Ghanem, and O. M. Knio. Multi-resolution analysis of Wiener-type uncertainty propagation schemes. *J. Comput. Phys.*, 197(2):502–531, 2004.
- [36] N. Lüthen, S. Marelli, and B. Sudret. Sparse polynomial chaos expansions: Literature survey and benchmark. *SIAM/ASA J. Uncertain. Quantif.*, 9(2):593–649, 2021.
- [37] S. Marelli, P.-R. Wagner, C. Lataniotis, and B. Sudret. Stochastic spectral embedding. *Int. J. Uncertain. Quantif.*, 11(2):25–47, 2021.
- [38] H. G. Matthies and A. Keese. Galerkin methods for linear and nonlinear elliptic stochastic partial differential equations. *Comput. Methods Appl. Mech. Engrg.*, 194(12-16):1295–1331, 2005.
- [39] J. Ochoa-Tapia and S. Whitaker. Momentum transfer at the boundary between a porous medium and a homogeneous fluid—I. Theoretical development. *Int. J. Heat Mass Transfer*, 38:2635–2646, 1995.
- [40] J. Ochoa-Tapia and S. Whitaker. Momentum transfer at the boundary between a porous medium and a homogeneous fluid—II. Comparison with experiment. *Int. J. Heat Mass Transfer*, 38:2647–2655, 1995.
- [41] S. Oladyshkin and W. Nowak. Data-driven uncertainty quantification using the arbitrary polynomial chaos expansion. *Reliab. Eng. Syst. Saf.*, 106:179 – 190, 2012.
- [42] A. B. Owen. Sobol’ indices and Shapley value. *SIAM/ASA J. Uncertain. Quantif.*, 2(1):245–251, 2014.
- [43] R. Penrose. On best approximate solutions of linear matrix equations. In *Mathematical Proceedings of the Cambridge Philosophical Society*, volume 52, pages 17–19. Cambridge University Press, 1956.
- [44] P. Pettersson and H. A. Tchelepi. Stochastic Galerkin framework with locally reduced bases for nonlinear two-phase transport in heterogeneous formations. *Comput. Methods Appl. Mech. Engrg.*, 310:367–387, 2016.
- [45] G. Poëtte, B. Després, and D. Lucor. Uncertainty quantification for systems of conservation laws. *J. Comput. Phys.*, 228(7):2443–2467, 2009.
- [46] K. L. Ricciardi, G. F. Pinder, and K. Belitz. Comparison of the lognormal and beta distribution functions to describe the uncertainty in permeability. *J. Hydrology*, 313(3):248–256, 2005.
- [47] L. Ruan, I. Kröker, I. Rybak, and S. Oladyshkin. Replication data for: Surrogate-assisted global sensitivity analysis for hybrid-dimensional Stokes–Brinkman–Darcy model, 2025. doi: 10.18419/DARUS-5251.
- [48] L. Ruan and I. Rybak. Stokes–Brinkman–Darcy models for coupled free–flow and porous–medium systems. In E. Franck and et al., editors, *Finite Volumes for Complex Applications X – Volume 1, Elliptic and Parabolic Problems*, volume 432 of *Springer Proceedings in Mathematics & Statistics*, pages 365–373, 2023.
- [49] L. Ruan and I. Rybak. A hybrid-dimensional Stokes–Brinkman–Darcy model for arbitrary flows to the fluid–porous interface. *Transp. Porous Media*, 152:75, 2025.
- [50] L. Ruan and I. Rybak. Stokes–Brinkman–Darcy models for fluid–porous systems: derivation, analysis and validation. *Appl. Math. Comp.*, 510:129687, 2026.
- [51] P. G. Saffman. On the boundary condition at the surface of a porous medium. *Stud. Appl. Math.*, 50:93–101, 1971.
- [52] R. Schobi, B. Sudret, and J. Wiart. Polynomial-chaos-based kriging. *Int. J. Uncertain. Quantif.*, 5(2):171–193, 2015.
- [53] L. S. Shapley. A value for n -person games. In *Contributions to the theory of games, vol. 2*, volume no. 28 of *Ann. of Math. Stud.*, pages 307–317. Princeton Univ. Press, Princeton, NJ, 1953.
- [54] I. M. Sobol’. On the distribution of points in a cube and the approximate evaluation of integrals. *Zhurnal Vychislitel’noi Matematiki i Matematicheskoi Fiziki*, 7(4):784–802, 1967.
- [55] I. M. Sobol. Estimation of the sensitivity of nonlinear mathematical models. *Mat. Model.*, 2(1):112–118, 1990.

- [56] I. M. Sobol. Global sensitivity indices for nonlinear mathematical models and their Monte Carlo estimates. *Math. Comput. Simulation*, 55:271–280, 2001.
- [57] P. Strohbeck, E. Eggenweiler, and I. Rybak. A modification of the Beavers–Joseph condition for arbitrary flows to the fluid–porous interface. *Transp. Porous Media*, 147:605–628, 2023.
- [58] Y. Sudhakar, U. Lacin, S. Pasche, and S. Bagheri. Higher-order homogenized boundary conditions for flows over rough and porous surfaces. *Transp. Porous Media*, 136:1–42, 2021.
- [59] B. Sudret. Global sensitivity analysis using polynomial chaos expansions. *Reliab. Eng. Syst. Saf.*, 93(7):964–979, 2008.
- [60] T. J. Sullivan. *Introduction to Uncertainty Quantification*. Springer, 2015.
- [61] J. Tryoen, O. Le Maître, and A. Ern. Adaptive anisotropic spectral stochastic methods for uncertain scalar conservation laws. *SIAM J. Sci. Comput.*, 34(5):A2459–A2481, 2012.
- [62] K. Vafai. *Handbook of Porous Media*. CRC Press, 2005.
- [63] P.-R. Wagner, S. Marelli, I. Papaioannou, D. Straub, and B. Sudret. Rare event estimation using stochastic spectral embedding. *Structural Safety*, 96:102179, 2022.
- [64] X. Wan and G. E. Karniadakis. Multi-element generalized polynomial chaos for arbitrary probability measures. *SIAM J. Sci. Comput.*, 28(3):901–928, 2006.
- [65] N. Wiener. The homogeneous chaos. *Amer. J. Math.*, 60(4):897–936, 1938.
- [66] D. Xiu and G. E. Karniadakis. The Wiener-Askey polynomial chaos for stochastic differential equations. *SIAM J. Sci. Comput.*, 24(2):619–644, 2002.
- [67] D. Xiu and G. E. Karniadakis. Modeling uncertainty in flow simulations via generalized polynomial chaos. *J. Comput. Phys.*, 187(1):137–167, 2003.
- [68] G. A. Zampogna and F. Gallaire. Effective stress jump across membranes. *J. Fluid Mech.*, 892:A9, 2020.

APPENDIX A. SUPPLEMENTARY TABLES AND FIGURES

In this section, we provide additional tabulated data supporting the results of GSA presented in Sections 4.1.3 and 4.2.3. In particular, Tab. 6 reports the total sensitivity indices computed with aMR-PC for different choices of polynomial degree N_o , refinement level N_r , and sparsity by hyperbolic truncation parameter q for the filtration problem (Case 1). The corresponding results for the splitting flow problem (Case 2) are summarized in Tab. 9. Furthermore, Tabs. 7 and 8 present the space-averaged Sobol’ indices of the tangential velocity u and normal velocity v , respectively, for Case 1, while Tabs. 10 and 11 report the corresponding results for Case 2.

TABLE 6. Case 1: Averaged total sensitivity indices.

(A) Horizontal velocity component u .

	$N_o = 2$	$N_o = 4$	$N_o = 4/q = 0.75$	$N_r = 1/N_o = 2$	$N_r = 1/N_o = 4$	$N_r = 1/N_o = 4/q = 0.75$
$I = 1$	5.18e-01	1.93e-01	3.00e-02	5.05e-01	2.32e-01	6.91e-02
$I = 2$	1.85e-01	7.46e-01	1.41e-02	2.70e-01	9.57e-01	3.86e-02
$I = 3$	1.74e-01	1.13e-01	6.96e-02	1.97e-01	1.76e-01	3.20e-02
$I = 4$	1.18e-02	1.29e-02	8.77e-02	1.78e-02	1.04e-01	2.29e-02
$I = 5$	1.91e-01	3.14e-02	6.25e-02	1.78e-01	1.59e-01	2.55e-02

(B) Vertical velocity component v .

	$N_o = 2$	$N_o = 4$	$N_o = 4/q = 0.75$	$N_r = 1/N_o = 2$	$N_r = 1/N_o = 4$	$N_r = 1/N_o = 4/q = 0.75$
$I = 1$	4.87e-01	1.94e-01	2.80e-02	4.77e-01	2.42e-01	6.75e-02
$I = 2$	1.77e-01	7.29e-01	1.37e-02	2.62e-01	9.58e-01	3.86e-02
$I = 3$	1.63e-01	1.18e-01	6.65e-02	1.82e-01	1.72e-01	3.07e-02
$I = 4$	1.19e-02	1.35e-02	8.45e-02	1.77e-02	1.03e-01	2.26e-02
$I = 5$	1.87e-01	3.10e-02	6.20e-02	1.74e-01	1.61e-01	2.44e-02

TABLE 7. Case 1: Averaged Sobol' sensitivity indices.

(A) Horizontal velocity component u .

	$N_o = 2$	$N_o = 4$	$N_o = 4/q = 0.75$	$N_r = 1/N_o = 2$	$N_r = 1/N_o = 4$	$N_r = 1/N_o = 4/q = 0.75$
$I = 1$	4.17e-01	1.06e-01	1.93e-02	3.53e-01	6.47e-03	2.54e-02
$I = 12$	1.91e-02	3.99e-02	4.45e-04	3.49e-02	9.37e-02	1.62e-02
$I = 123$	0.00e+00	1.29e-03	0.00e+00	4.40e-03	2.35e-02	4.57e-04
$I = 1234$	0.00e+00	9.11e-05	0.00e+00	3.97e-04	4.03e-03	1.55e-03
$I = 12345$	0.00e+00	0.00e+00	0.00e+00	7.28e-04	4.85e-02	1.28e-03
$I = 1235$	0.00e+00	1.94e-05	0.00e+00	2.35e-04	1.47e-02	1.55e-03
$I = 124$	0.00e+00	7.79e-04	0.00e+00	7.13e-04	6.29e-03	2.34e-03
$I = 1245$	0.00e+00	8.92e-07	0.00e+00	1.69e-04	2.11e-02	9.65e-04
$I = 125$	0.00e+00	7.66e-04	0.00e+00	3.92e-03	1.07e-02	2.85e-03
$I = 13$	5.02e-02	3.92e-02	0.00e+00	7.77e-02	2.41e-03	3.74e-03
$I = 134$	0.00e+00	1.18e-04	0.00e+00	2.99e-04	1.48e-05	3.59e-03
$I = 1345$	0.00e+00	5.32e-06	0.00e+00	7.69e-05	1.01e-05	1.29e-03
$I = 135$	0.00e+00	2.29e-05	0.00e+00	6.05e-05	4.05e-06	1.59e-03
$I = 14$	2.18e-03	2.11e-03	8.69e-04	4.34e-03	1.59e-04	2.81e-03
$I = 145$	0.00e+00	5.05e-05	0.00e+00	1.27e-04	8.00e-06	1.02e-03
$I = 15$	2.90e-02	3.34e-03	9.36e-03	2.42e-02	2.63e-04	2.48e-03
$I = 2$	1.47e-01	6.70e-01	7.58e-04	1.87e-01	6.03e-01	8.70e-03
$I = 23$	1.22e-02	2.29e-02	1.35e-05	1.59e-02	6.01e-02	8.82e-04
$I = 234$	0.00e+00	2.12e-04	0.00e+00	2.16e-04	5.70e-03	6.39e-04
$I = 2345$	0.00e+00	1.17e-06	0.00e+00	2.33e-04	2.07e-03	1.13e-05
$I = 235$	0.00e+00	2.33e-04	0.00e+00	1.89e-04	1.23e-02	7.66e-06
$I = 24$	1.21e-03	5.10e-03	1.29e-02	1.60e-03	6.37e-03	4.87e-04
$I = 245$	0.00e+00	1.13e-04	0.00e+00	1.48e-04	9.38e-03	4.38e-05
$I = 25$	5.66e-03	4.23e-03	0.00e+00	1.90e-02	3.61e-02	6.19e-04
$I = 3$	1.12e-01	4.84e-02	8.73e-04	9.60e-02	2.58e-03	9.96e-03
$I = 34$	2.59e-05	1.99e-05	6.82e-02	8.20e-05	3.19e-06	5.47e-03
$I = 345$	0.00e+00	3.75e-06	0.00e+00	4.73e-05	2.20e-06	1.45e-05
$I = 35$	3.89e-05	2.07e-05	5.51e-04	4.19e-05	2.05e-06	1.46e-05
$I = 4$	8.25e-03	4.21e-03	3.95e-03	8.49e-03	2.69e-04	1.21e-03
$I = 45$	1.24e-04	7.41e-05	1.88e-03	1.55e-04	7.36e-06	2.07e-04
$I = 5$	1.57e-01	2.25e-02	5.07e-02	1.29e-01	4.27e-03	1.16e-02

TABLE 8. Case 1: Averaged Sobol' sensitivity indices.

(A) Vertical velocity component v .

	$N_o = 2$	$N_o = 4$	$N_o = 4/q = 0.75$	$N_r = 1/N_o = 2$	$N_r = 1/N_o = 4$	$N_r = 1/N_o = 4/q = 0.75$
$I = 1$	3.89e-01	9.73e-02	1.74e-02	3.30e-01	6.09e-03	2.31e-02
$I = 12$	2.00e-02	4.73e-02	4.59e-04	3.62e-02	1.07e-01	1.66e-02
$I = 123$	0.00e+00	1.33e-03	0.00e+00	4.13e-03	2.30e-02	4.68e-04
$I = 1234$	0.00e+00	1.01e-04	0.00e+00	3.71e-04	3.63e-03	1.57e-03
$I = 12345$	0.00e+00	0.00e+00	0.00e+00	6.48e-04	4.67e-02	1.22e-03
$I = 1235$	0.00e+00	2.36e-05	0.00e+00	2.12e-04	1.38e-02	1.56e-03
$I = 124$	0.00e+00	8.52e-04	0.00e+00	6.86e-04	5.33e-03	2.44e-03
$I = 1245$	0.00e+00	1.04e-06	0.00e+00	1.45e-04	2.16e-02	9.20e-04
$I = 125$	0.00e+00	8.45e-04	0.00e+00	3.95e-03	1.20e-02	3.09e-03
$I = 13$	4.71e-02	4.04e-02	0.00e+00	7.23e-02	2.45e-03	3.60e-03
$I = 134$	0.00e+00	1.31e-04	0.00e+00	3.04e-04	1.58e-05	3.52e-03
$I = 1345$	0.00e+00	4.83e-06	0.00e+00	6.89e-05	9.97e-06	1.22e-03
$I = 135$	0.00e+00	2.18e-05	0.00e+00	5.06e-05	3.94e-06	1.60e-03
$I = 14$	2.18e-03	2.24e-03	8.74e-04	4.31e-03	1.69e-04	2.93e-03
$I = 145$	0.00e+00	5.39e-05	0.00e+00	1.26e-04	8.49e-06	9.75e-04
$I = 15$	2.87e-02	3.54e-03	9.26e-03	2.41e-02	2.86e-04	2.63e-03
$I = 2$	1.39e-01	6.43e-01	7.49e-04	1.80e-01	5.89e-01	8.05e-03
$I = 23$	1.15e-02	2.58e-02	1.03e-05	1.48e-02	5.83e-02	8.38e-04
$I = 234$	0.00e+00	2.37e-04	0.00e+00	2.05e-04	5.31e-03	6.21e-04
$I = 2345$	0.00e+00	1.03e-06	0.00e+00	1.97e-04	2.07e-03	1.12e-05
$I = 235$	0.00e+00	2.43e-04	0.00e+00	1.56e-04	1.38e-02	7.40e-06
$I = 24$	1.15e-03	5.02e-03	1.25e-02	1.61e-03	6.50e-03	4.84e-04
$I = 245$	0.00e+00	1.16e-04	0.00e+00	1.32e-04	1.09e-02	4.59e-05
$I = 25$	5.56e-03	4.00e-03	0.00e+00	1.89e-02	3.81e-02	6.62e-04
$I = 3$	1.04e-01	4.96e-02	9.22e-04	8.80e-02	2.59e-03	9.30e-03
$I = 34$	3.61e-05	1.92e-05	6.50e-02	7.92e-05	3.09e-06	5.16e-03
$I = 345$	0.00e+00	4.28e-06	0.00e+00	4.42e-05	2.26e-06	1.42e-05
$I = 35$	1.01e-05	1.30e-05	5.85e-04	1.60e-05	1.68e-06	1.25e-05
$I = 4$	8.45e-03	4.64e-03	4.11e-03	8.60e-03	2.95e-04	1.24e-03
$I = 45$	1.23e-04	7.98e-05	1.97e-03	1.49e-04	7.89e-06	2.17e-04
$I = 5$	1.52e-01	2.21e-02	5.02e-02	1.25e-01	2.18e-03	1.02e-02

TABLE 9. Case 2: Averaged total sensitivity indices.

(A) Horizontal velocity component u .

	$N_o = 2$	$N_o = 4$	$N_o = 4/q = 0.75$	$N_r = 1/N_o = 2$
$I = 1$	3.01e-01	1.55e-01	2.83e-02	3.09e-01
$I = 2$	7.35e-02	3.01e-01	1.37e-02	8.74e-02
$I = 3$	1.70e-01	9.82e-02	6.45e-02	1.98e-01
$I = 4$	1.12e-02	8.29e-03	8.17e-02	1.78e-02
$I = 5$	4.87e-01	4.84e-01	4.93e-01	4.89e-01

(B) Vertical velocity component v .

	$N_o = 2$	$N_o = 4$	$N_o = 4/q = 0.75$	$N_r = 1/N_o = 2$
$I = 1$	2.94e-01	1.55e-01	2.80e-02	3.02e-01
$I = 2$	7.18e-02	2.92e-01	1.33e-02	8.53e-02
$I = 3$	1.66e-01	9.75e-02	6.29e-02	1.93e-01
$I = 4$	1.09e-02	8.62e-03	7.97e-02	1.74e-02
$I = 5$	4.75e-01	4.70e-01	4.80e-01	4.76e-01

TABLE 10. Case 2: Averaged Sobol' sensitivity indices.

(A) Horizontal velocity component u .

	$N_o = 2$	$N_o = 4$	$N_o = 4/q = 0.75$	$N_r = 1/N_o = 2$
$I = 1$	2.45e-01	1.01e-01	1.95e-02	2.12e-01
$I = 12$	1.43e-03	1.02e-02	4.42e-04	2.22e-03
$I = 123$	0.00e+00	1.39e-03	0.00e+00	4.85e-03
$I = 1234$	0.00e+00	8.67e-05	0.00e+00	4.33e-04
$I = 12345$	0.00e+00	0.00e+00	0.00e+00	7.08e-04
$I = 1235$	0.00e+00	9.38e-06	0.00e+00	1.88e-04
$I = 124$	0.00e+00	1.88e-04	0.00e+00	7.27e-04
$I = 1245$	0.00e+00	2.46e-08	0.00e+00	1.93e-04
$I = 125$	0.00e+00	8.44e-05	0.00e+00	1.62e-04
$I = 13$	5.15e-02	3.93e-02	0.00e+00	8.15e-02
$I = 134$	0.00e+00	1.13e-04	0.00e+00	3.02e-04
$I = 1345$	0.00e+00	4.70e-06	0.00e+00	8.46e-05
$I = 135$	0.00e+00	4.21e-05	0.00e+00	7.10e-05
$I = 14$	2.42e-03	2.20e-03	9.16e-04	4.83e-03
$I = 145$	0.00e+00	5.26e-05	0.00e+00	1.36e-04
$I = 15$	3.33e-04	2.69e-04	7.46e-03	3.89e-04
$I = 2$	5.84e-02	2.73e-01	8.04e-04	5.89e-02
$I = 23$	1.23e-02	1.24e-02	1.37e-05	1.61e-02
$I = 234$	0.00e+00	1.86e-04	0.00e+00	2.11e-04
$I = 2345$	0.00e+00	9.06e-07	0.00e+00	2.47e-04
$I = 235$	0.00e+00	3.96e-05	0.00e+00	2.15e-04
$I = 24$	1.26e-03	1.83e-03	1.24e-02	1.77e-03
$I = 245$	0.00e+00	1.06e-04	0.00e+00	1.47e-04
$I = 25$	1.12e-04	1.46e-03	0.00e+00	2.74e-04
$I = 3$	1.06e-01	4.44e-02	7.69e-04	9.27e-02
$I = 34$	2.69e-05	1.89e-05	6.32e-02	8.47e-05
$I = 345$	0.00e+00	9.13e-07	0.00e+00	4.67e-05
$I = 35$	1.02e-04	1.21e-04	4.86e-04	1.15e-04
$I = 4$	7.35e-03	3.41e-03	3.47e-03	7.71e-03
$I = 45$	1.12e-04	8.18e-05	1.65e-03	1.56e-04
$I = 5$	4.86e-01	4.82e-01	4.83e-01	4.85e-01

TABLE 11. Case 2: Averaged Sobol' sensitivity indices.

(A) Vertical velocity component v .

	$N_o = 2$	$N_o = 4$	$N_o = 4/q = 0.75$	$N_r = 1/N_o = 2$
$I = 1$	2.39e-01	1.01e-01	1.92e-02	2.07e-01
$I = 12$	1.21e-03	1.01e-02	4.51e-04	2.11e-03
$I = 123$	0.00e+00	1.37e-03	0.00e+00	4.68e-03
$I = 1234$	0.00e+00	8.72e-05	0.00e+00	4.01e-04
$I = 12345$	0.00e+00	0.00e+00	0.00e+00	6.84e-04
$I = 1235$	0.00e+00	8.95e-06	0.00e+00	1.46e-04
$I = 124$	0.00e+00	1.91e-04	0.00e+00	7.05e-04
$I = 1245$	0.00e+00	1.90e-08	0.00e+00	1.54e-04
$I = 125$	0.00e+00	8.58e-05	0.00e+00	1.37e-04
$I = 13$	5.05e-02	3.89e-02	0.00e+00	7.98e-02
$I = 134$	0.00e+00	1.20e-04	0.00e+00	2.99e-04
$I = 1345$	0.00e+00	4.84e-06	0.00e+00	7.32e-05
$I = 135$	0.00e+00	3.21e-05	0.00e+00	6.49e-05
$I = 14$	2.43e-03	2.31e-03	9.35e-04	4.89e-03
$I = 145$	0.00e+00	5.44e-05	0.00e+00	1.36e-04
$I = 15$	5.30e-04	3.26e-04	7.40e-03	5.61e-04
$I = 2$	5.69e-02	2.64e-01	7.50e-04	5.76e-02
$I = 23$	1.22e-02	1.27e-02	9.88e-06	1.60e-02
$I = 234$	0.00e+00	1.95e-04	0.00e+00	1.90e-04
$I = 2345$	0.00e+00	9.36e-07	0.00e+00	2.03e-04
$I = 235$	0.00e+00	3.83e-05	0.00e+00	1.86e-04
$I = 24$	1.28e-03	1.88e-03	1.21e-02	1.76e-03
$I = 245$	0.00e+00	9.73e-05	0.00e+00	1.00e-04
$I = 25$	1.25e-04	1.05e-03	0.00e+00	3.64e-04
$I = 3$	1.04e-01	4.40e-02	7.56e-04	9.05e-02
$I = 34$	1.55e-05	1.60e-05	6.17e-02	6.14e-05
$I = 345$	0.00e+00	8.93e-07	0.00e+00	4.26e-05
$I = 35$	4.80e-05	4.86e-05	4.81e-04	5.47e-05
$I = 4$	7.06e-03	3.59e-03	3.35e-03	7.52e-03
$I = 45$	1.07e-04	7.27e-05	1.61e-03	1.47e-04
$I = 5$	4.74e-01	4.68e-01	4.70e-01	4.73e-01